



An advanced modelling study on the role of dimethyl sulfide in new particle formation in the pristine marine boundary layer

Robin Wollesen de Jonge¹, Zihao Fu^{1,2}, Pontus Roldin³, and Michael Boy^{1,4,5}

¹Institute for Atmospheric and Earth Systems Research, University of Helsinki, FI-00014 Helsinki, Finland

²State Key Laboratory of Regional Environment and Sustainability, International Joint Laboratory for Regional Pollution Control, Ministry of Education (IJRC), College of Environmental Sciences and Engineering, Peking University, CN-100871 Beijing, China

³Department of Physics, Lund University, Lund SE-22363, Sweden

⁴Atmospheric Modelling Centre – Lahti, Lahti University Campus, FI-15110 Lahti, Finland

⁵School of Engineering Sciences, Lappeenranta-Lahti University of Technology LUT, Lahti FI-15110, Finland

Correspondence: Robin Wollesen de Jonge (robin.wollesendejonge@helsinki.fi)

Abstract.

New particle formation (NPF) enhances the concentration of cloud condensation nuclei (CCN) over the oceans, thereby affecting the radiative balance and, consequently, Earth's climate. The literature suggest that marine NPF predominantly occurs in the free troposphere, as the extensive surface area of sea spray aerosols and limited precursor gases suppress NPF in the marine boundary layer (MBL). However, such interpretations do not fully account for the observations on nucleation and Aitken-mode particles within the MBL. Here, we demonstrate how natural emissions of dimethyl sulfide (DMS) and NH₃ can drive H₂SO₄-NH₃-derived NPF in the MBL during cloud-free conditions following precipitation events. The newly formed particles manage to grow into the upper Aitken and accumulation mode size range within 3-4 days, with the potential to act as CCN. Through extensive sensitivity runs, we show that DMS-derived NPF and growth exhibits a non-linear response to variations in air temperature and wind speed, whereas their response to changes in sea surface temperature, precipitation rate, and DMS surface ocean concentration remains approximately linear. Sporadic cloud cover is shown to suppress NPF. Finally, we report new rate coefficients and reaction pathways for the OH-initiated oxidation of methane sulphinic acid (MSIA) and assess key uncertainties in the DMS oxidation mechanism, illustrating their impact on the formation and growth of DMS-derived aerosol particles in the MBL.

15

1 Introduction

Cloud condensation nuclei (CCN) over the oceans impact the formation, albedo and lifetime of marine clouds and thereby the global climate system (Charlson et al., 1987; Rosenfeld et al., 2019). The formation of aerosol particles through vapour nucleation, namely new particle formation (NPF) (Kulmala et al., 2013), is believed to give rise to more than half of the CCN



20 in the marine boundary layer (MBL) (Merikanto et al., 2009). Observations on NPF in the MBL nevertheless remains scarce, and while certain studies report NPF events during cruise (Baccarini et al., 2021) and flight campaigns (Zheng et al., 2021), it is commonly believed that such events are rare (Pirjola et al., 2000; Quinn and Bates, 2011). Instead, aerosol particles are thought to enter the MBL from the free troposphere, in which low temperatures and low particle concentrations provides more favourable conditions for NPF (Williamson et al., 2019). While the question of open ocean NPF remains ambiguous, measurements made at coastal sites frequently show NPF (Jokinen et al., 2018; Dall'Osto et al., 2018; Beck et al., 2021; Brean et al., 2021)

Throughout the atmosphere, vapours with strong intermolecular interactions can undergo nucleation to form clusters that may grow into aerosol particles (Elm et al., 2020). One such vapour is sulfuric acid (SA: H_2SO_4), which is known to nucleate in the presence of a stabilizing base such as NH_3 (Korhonen et al., 1999; Kirkby et al., 2011). Over the oceans, dimethyl sulfide (DMS: $(\text{CH}_3)_2\text{S}$) emitted from phytoplankton comprises the largest source of natural sulfur and thus SA to the atmosphere (Lovelock et al., 1972; Bates et al., 1992). DMS therefore has the potential to influence NPF and CCN concentrations in the marine environment (Charlson et al., 1987; Rosati et al., 2021) and over land (Wollesen de Jonge et al., 2024), although its role in said processes remains to be fully understood. One of the main shortcomings in our current understanding concerns the oxidation mechanism of DMS, which has undergone extensive revision in recent years (Jacob et al., 2024). DMS oxidation is driven by O_3 , HO_x , NO_x and halogen radicals in both the gas-phase and the aqueous-phase of deliquesced aerosol particles and cloud droplets, where it forms the stable species dimethyl sulfoxide (DMSO: CH_3SOCH_3), methane sulphinic acid (MSIA: $\text{CH}_3\text{SO}_2\text{H}$), methanesulfonic acid (MSA: $\text{CH}_3\text{SO}_3\text{H}$) and sulfur dioxide (SO_2) in addition to SA (Barnes et al., 2006; Hoffmann et al., 2016; Wollesen de Jonge et al., 2021). DMS has also been found to undergo autoxidation to form hydroperoxymethyl thioformate (HPMTF: $\text{HOOCH}_2\text{SCHO}$) (Wu et al., 2014; Berndt et al., 2019; Ye et al., 2022). Although heavily researched, many of the reactions pathways forming said compounds remain uncertain, with large variations in the reaction rates presented in the literature. These uncertainties influence the distribution of products from DMS oxidation, making it difficult to assess the impact of DMS on the formation and growth of aerosol particles in the atmosphere - including the impact of DMS on NPF within the MBL.

45

Here, we use advanced process-based modelling to demonstrate the role of DMS in NPF and secondary aerosol growth within the pristine MBL. For this purpose, we construct an open ocean scenario in the box model ADCHAM and examine DMS-driven NPF under different meteorological and hydrological conditions, including cloud and non-cloud periods, precipitation events and varying wind-speeds, air temperatures, sea surface temperatures and sea surface concentrations of dissolved DMS and NH_x . In addition to ADCHAM, we also include the use of detailed quantum chemical calculations to address uncertainties and alternative reaction pathways in the DMS oxidation mechanism. This is done as a means to reduce the uncertainty related to the role of DMS in NPF over the oceans.

50



2 Methods

2.1 Model Description

55 Simulations were performed in the gas and particle phase chemistry box model ADCHAM (Roldin et al., 2014). ADCHAM considers state-of-the-art aerosol dynamics, treating the formation, growth, ageing and deposition of aerosol particles in the atmosphere. New particles are formed in the model by use of the Atmosphere Cluster Dynamics Code (ACDC) (McGrath et al., 2012; Olenius et al., 2013). ACDC takes into account both neutral and ion-induced pathways when calculating nucleation rates for various clustering systems, simulating the formation of clusters consisting of maximum five acid molecules and five base
60 molecules. Clusters that manage to grow into the upper size range in ACDC are introduced as particles in ADCHAM in the smallest size bin at 1.08 nm. The setup used in this study models NPF from SA and NH₃, taking into account the loss of clusters to collisions, evaporation, coagulation, and scavenging. The SA-NH₃ system was calculated using the DLPNO method at the DLPNO-CCSD(T)/aug-cc-pVTZ// ω B97X-D/6-31++G(d,p) quantum chemical level of theory (Besel et al., 2020). The DLPNO method was used in the default model setup as opposed to the RI-CC2 method as RI-CC2 has been shown to over-
65 predict cluster binding energies (Schmitz and Elm, 2020). Nucleation rates obtained with the RI-CC2 method should therefore be interpreted as the upper limit for SA-NH₃ driven NPF, whereas nucleation rates obtained with the DLPNO method comprises the lower (and more realistic) limit.

Newly formed or pre-existing aerosol particles grow in the model, either through vapour condensation or through the parti-
70 tioning and processing of water soluble species in the deliquesced aerosol particles and cloud droplets. The condensation and evaporation of species is solved with the analytical predictor of condensation (APC) scheme (Jacobson, 2005), taking into account the dissociation of condensing compounds in the aerosol particle aqueous-phase. Other water soluble compounds, including oxidation agents, are allowed to partition to and (for certain compounds) dissociate in the aqueous-phase in accordance with their Henry's law solubility and pKa values, respectively. In this study, ADCHAM considers the partitioning of 52
75 gaseous species to the aerosol particle aqueous-phase. Some of these species contribute to the growth of the aerosol particles by undergoing aqueous-phase oxidation to form low-volatile compounds that remain in the particle-phase upon a decrease in the aerosol particle deliquescence or the evaporation of cloud droplets. Henry's law solubilities and pKa values for the key DMS-derived water-soluble compounds HPMTF, DMSO, MSIA and MSA are based on COSMO_{therm} (cos, 2021) calculations obtained from Wollesen de Jonge et al. (2024).

80 Once formed, aerosol particles in ADCHAM leave the atmosphere through either wet or dry-deposition. Wet-deposition, including bellow cloud-scattering of particles, is calculated for different particle sizes in accordance with the parameterization by Laakso et al. (2003). The parameterization considers the intensity of precipitation in mm/h. Dry-deposition of aerosol particles in an ocean environment relevant for this study is calculated with the parameterization by Slinn and Slinn (1980).

85



To investigate the influence of DMS on NPF in the pristine MBL, a model scenario reproducing conditions over the remote open ocean was constructed. In the BaseCase scenario, the movement of an air-parcel within the MBL is simulated for 144 hours, starting and ending at midnight. During the first 48 hours, the air-parcel passes through cloud cover four times - twice during midnight and twice during mid-day. To form clouds, the air-parcel is lifted, causing the air to become supersaturated with respect to water vapour through adiabatic cooling. The clouds are allowed to persist for two hours, until the air-parcel descends and they evaporate. During the fourth cloud event, heavy precipitation at 10 mm/h is introduced in the model. The cloud is allowed to precipitate for the first hour of its lifetime. During the remaining four days of the simulation, no cloud or precipitation events take place. In this time (and in between cloud periods during the first two days), the relative humidity is kept at 90% and the aerosol particles are assumed to be deliquesced. The scenario is constructed to imitate the conditions during the flight-campaign described in Zheng et al. (2021), where frequent NPF within the MBL was observed following the passage of cold fronts.

The prescribed scenario is designed to spur NPF after the precipitation event on day three of the simulation. Before this event, the model is initiated with a size distribution consisting of NaCl in the accumulation and coarse mode in addition to $(\text{Na})_2\text{SO}_4$ in the Aitken mode. The initial aerosol concentration is kept high to ensure that new particles are less likely to form during the first two days of the simulation. The precipitation event on day two effectively lowers the aerosol particle concentration, allowing DMS-derived oxidation products to form and grow new particles. The initial size distribution and sea spray emissions are calculated using the parameterization by Salter et al. (2015). This parameterization takes into account the surface layer wind-speed, which is kept fixed at 6 m/s in the BaseCase simulation but varied in additional sensitivity runs.

DMS emissions in ADCHAM are treated by considering an oceanic DMS dataset and a DMS transfer velocity parameterization. The oceanic DMS dataset by Lana et al. (2011) was used to construct four scenarios with five different surface ocean concentrations of DMS, including low (5 nmol/L), moderate (10 nmol/L), high (15 nmol/L) and very high (20 nmol/L) concentrations. High to very high concentrations of DMS are representative for phytoplankton blooms in the North Atlantic Ocean during May-July, and in the Southern Ocean from December-February (Lana et al., 2011; Hulswar et al., 2022). It should be noted that even higher concentrations can be found in the ocean surrounding Antarctica during sea-ice breakout. A super-linear transfer velocity specifically made for DMS was used to obtain the flux of DMS to the model (Blomquist et al., 2017). We acknowledge that alternative linear and quadratic transfer velocities are also commonly used to calculate the DMS sea-air flux (Liss and Merlivat, 1986; Wanninkhof, 2014; Nightingale et al., 2000). All parameterizations consider the sea surface temperature (SST) and wind-speed when calculating the transfer velocity. Emissions of NH_3 were treated similar to DMS by considering an oceanic dataset and a transfer velocity. The sea surface concentration of total ammonium NH_x was set to 0.3 mmol/m³. This values represents a middle ground between NH_x concentrations observed in the North Atlantic Ocean (May-July: ~ 0.2 mmol/m³) and the Southern ocean around Antarctica (December-February: ~ 0.4 mmol/m³) when the phytoplankton blooms are at their peak in each respective region (Paulot et al., 2020). Additional sensitivity runs are performed using both higher and lower concentration of sea surface NH_x . The transfer velocity of NH_3 was calculated in accordance with

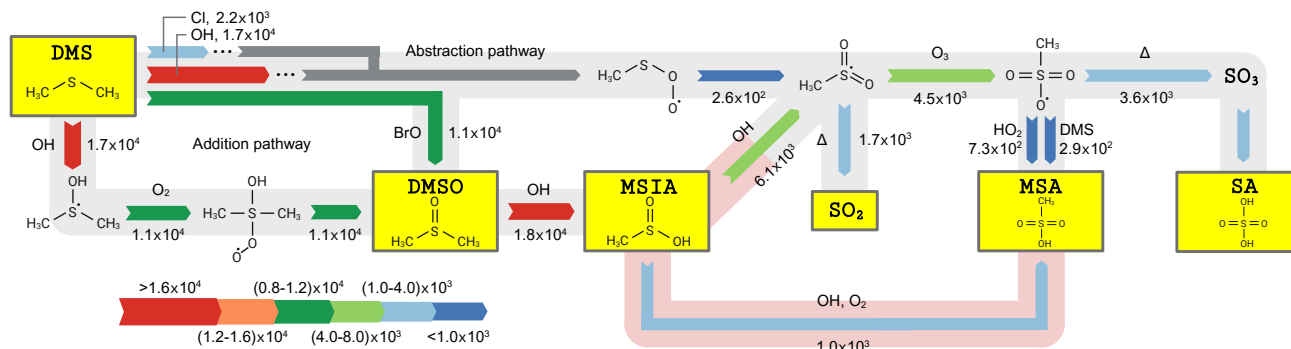


Figure 1. Simplified DMS oxidation mechanism for the gas-phase reactions responsible for the direct production of SA in the MBL. Source/sink fluxes for the respective compounds are reported in molecules cm⁻³ s⁻¹ and calculated at the conditions given in the BaseCase simulation. The fluxes are shown next to the arrow for each reaction together the reactant for said reaction. Key compounds, all of which are able to partition to the aqueous-phase, are highlighted in yellow. New and modified pathways are marked in red.

the method by Wentworth et al. (2016). It should be noted that the sea surface concentration of both NH_x and DMS can reach considerably higher concentrations near the coast, especially in regions with strong upwelling or nutrient run-off (Lana et al., 2011; Paulot et al., 2020; Hulswar et al., 2022). Emissions of biogenic volatile organic compounds (BVOCs) over the oceans (including isoprene and α -pinene) is treated in accordance with the rates reported in Hoffmann et al. (2016).

125 2.2 DMS Oxidation Mechanism

The DMS oxidation reaction scheme used in this study has its basis in the mechanism presented in Wollesen de Jonge et al. (2021). Here, this mechanism is updated to account for the recent advances in the representation of DMS chemistry. In addition to these updates, we also use quantum chemical calculations to present new reaction pathways and temperature dependencies, as a means to address reactions in the DMS oxidation mechanism that still remain uncertain. The full gas-phase and aqueous-
 130 phase mechanism is found in Table S1 and S2, respectively. A simplified scheme for the gas-phase reactions that impact the direct formation of SA and thus DMS-driven NPF in the MBL is shown in Figure 1.

The main part of the DMS-derived gas-phase chemistry is taken from the Master Chemical Mechanism version 3.3.1 (MCMv3.3.1) (Jenkin et al., 1997, 2003). This includes the gas-phase oxidation of DMS by OH and NO₃ in addition to the fundamental processing of oxidation intermediates and products in the so-called addition and abstraction pathway. Here, the addition pathway refers to the addition of OH to DMS while the abstraction pathway refers to the H-abstraction from DMS by OH. The oxidation
 135 of DMS by halogen radicals Cl and BrO (through H-abstraction and addition, respectively) is treated in accordance with the study by Hoffmann et al. (2016). The processing of halogen radicals, including the activation of chlorine and bromine species in the sea spray particles, is obtained from Brauer et al. (2013). This chemistry is essential for the representation of halogen



140 radicals in the MBL and thus the oxidation of DMS. In addition to the halogen driven oxidation of DMS, Hoffmann et al. (2016) also provides the reactions that govern the aqueous-phase processing of DMS and its water soluble oxidation products in both deliquesced aerosol particles and cloud droplets. Amongst others, these reactions include the uptake of DMS, DMSO and MSIA to the aqueous-phase and their reaction with OH and O₃ to form MSA. The uptake of MSIA has been found to be particularly impactful for the production of MSA particle mass (PM), as MSIA is able to partition to deliquesced aerosol
145 particles in between cloud periods (Hoffmann et al., 2016; Wollesen de Jonge et al., 2021). The aqueous-phase processing of SO₂ is treated in accordance with Jacobson (2005).

The formation of HPMTF through autoxidation, proposed in theory by Wu et al. (2014), shown first in experiments by Berndt et al. (2019) and observed in the atmosphere by Veres et al. (2020), has undergone numerous revisions in the last couple years.
150 The compound is formed from the CH₃SCH₂OO peroxy radical (produced initially in the DMS abstraction pathway), which undergoes two hydrogen shifts (H-shifts) to form HPMTF. The first of the two H-shift is considerably slower than the second and thus constitutes the rate-limiting step in the formation of HPMTF. Veres et al. (2020) used multiconformer transition state theory to calculate temperature dependant rate coefficients for both H-shifts. Using this approach, the first and rate-limiting H-shift was determined to be 0.047 s⁻¹ at 295K. This estimate remains considerably slower than the some of the reaction
155 coefficients determined in experiments, e.g. by Berndt et al. (2019) (0.23 ± 0.12 s⁻¹ at 295K) and Ye et al. (2022) (0.13 ± 0.03 s⁻¹ at 295K). In this study, we use the temperature dependant rate coefficient by Veres et al. (2020) and scale it to match the rate coefficient obtained by Ye et al. (2022). The rate by Ye et al. (2022) is used as opposed to the rate by Berndt et al. (2019), as the uncertainty associated with the rate is lower. To stay consistent with the use of reaction coefficient from Ye et al. (2022), the subsequent reaction of HPMTF with OH is also implemented from this study. Said rate is considerably higher than the
160 original one presented in the study by Wu et al. (2014) (2.1 × 10⁻¹¹ cm³ s⁻¹ and 1.4 × 10⁻¹² cm³ s⁻¹, respectively), ensuring that a higher fraction of HPMTF is converted to SO₂.

Another aspect of the DMS oxidation mechanism that has undergone revision in recent years is the fate of the products formed in the addition-pathway. In MCMv3.3.1, DMS undergoes OH addition to form DMSO, MSIA and finally SO₂. Recent stud-
165 ies, combining smog chamber experiments on DMS oxidation with box modelling, are nevertheless unable to account for the production of MSA in the gas-phase and particle-phase without considering the H-abstraction from MSIA by OH to form the intermediate radical CH₃SO₂ (Wollesen de Jonge et al., 2021; Shen et al., 2022). CH₃SO₂ subsequently undergoes thermal decomposition to form SO₂ (similar to the fate of MSIA in MCMv3.3.1), but may also react with O₃ or O₂ and NO to form CH₃SO₃ and thus SA and MSA. Here it is essential to distinguish between the formation of SA from CH₃SO₃ and from SO₂,
170 the latter pathway being considerably slower than the first (2.8 × 10⁻² s⁻¹ and 8.8 × 10⁻⁷ s⁻¹ at 283K and an OH concentration of 10⁶ cm⁻³). With a direct impact on the production of SA and MSA, the H-abstraction from MSIA by OH therefore has the potential to impact the formation and growth of aerosol particles in the MBL. The reaction coefficient for said reaction was set to match the experimentally determined rate by Kukui et al. (2003). As this rate was determined at 298K, quantum chemical calculations are used in this study to provide temperature dependency for the reaction (section 2.4). These calculations demon-



175 strate that the H-abstraction is more likely to occur at lower temperatures. While the H-abstraction from MSIA by OH has
been shown to improve the model representation of MSA in previous publications, others continue to report a missing source
of MSA in their model simulations (Ye et al., 2022). Consequently, this study also includes the addition of OH to MSIA, ulti-
mately forming MSA through O₂ hydrogen abstraction. This pathway has been proposed theoretically in previous publications
(Lucas and Prinn, 2002; Shen et al., 2022; Ye et al., 2022), but the rate of reaction has so far only been based on estimates or
180 taken from similar reactions. Here, we implement quantum chemical calculations to determine the temperature dependant rate
coefficient for the production of MSA through OH addition to MSIA. The reaction pathway is incorporated together with the
work by Lv et al. (2019), which suggest that H₂SO₃ also forms from the addition of OH to MSIA. In this mechanism, H₂SO₃
is assumed to decompose directly to SO₂. An alternative source of MSA through the reaction of CH₃SO₃ with DMS is also
considered (Yin et al., 1990; Jacob et al., 2024).

185

The isomerization of CH₃SOO to CH₃SO₂ was included in the mechanism in accordance with the study by Hoffmann et al.
(2016), which ensures that SA and MSA forms in the abstraction pathway, even during low NO_x conditions (Turnipseed et al.,
1995; Lucas and Prinn, 2002). In MCMv3.3.1, CH₃SO₂ is only able to form via the abstraction pathway through the reaction
of CH₃SO with NO₂ or via O₂ addition followed by oxygen abstraction by NO. As NO_x concentrations are known to be low
190 in the pristine MBL, the isomerization of CH₃SOO therefore plays a role in the production of CH₃SO₂, SA and thus NPF.
The fate of CH₃SO₂ nevertheless remains uncertain. CH₃SO₂ either undergoes thermal decomposition to form SO₂ or reacts
with O₃, NO₂ or O₂ followed by NO to form CH₃SO₃. While the reaction coefficients for the reactions forming CH₃SO₃ are
consistent in the literature, the coefficient for the thermal decomposition of CH₃SO₂ are not. MCMv3.3.1 reports a temperature
dependant reaction coefficient of 0.29 s⁻¹ at 295K, which is considerably lower than the estimates used in the box modelling
195 studies by Jacob et al. (2024) (6 s⁻¹ at 295K) and Berndt et al. (2023) (20 s⁻¹ at 295K). As the two latter reaction coefficients
are in fact estimates obtained by fitting box model results to measurements, the rate presented in MCMv3.3.1 is used in this
study. Due to the impact of the reaction on the distribution of SO₂, SA and MSA (and thereby NPF), the different rates
are tested in ADCHAM through sensitivity runs. Similar to CH₃SO₂, the thermal decomposition of CH₃SO₃ also remains
uncertain. Again, MCMv3.3.1 reports a relatively low rate for the reaction (0.11 s⁻¹ at 295K) while another study suggests
200 that the reaction coefficient might be considerably higher (9.71 s⁻¹ at 295K) (Cao et al., 2013). The rate from MCMv3.3.1 is
implemented as the default rate in this study while sensitivity runs are performed with the rate by Cao et al. (2013).

2.3 Sensitivity Runs

In addition to the default simulation (named BaseCase), different sensitivity runs were performed to test the impact of me-
teorological and hydrological conditions along with alternative rate coefficients and reaction pathways in the DMS oxidation
205 mechanism on the role of DMS in NPF in the MBL. Table 1 gives an overview of the different simulations. The TEMP₂₇₃,
TEMP₂₇₈, TEMP₂₈₈ and TEMP₂₉₃ sensitivity runs are performed at air temperatures both lower and higher than in the Base-
Case simulation, respectively. This is done to demonstrate the impact of temperature on the DMS chemistry in addition to its
effect on particle formation and particle growth. WS₂, WS₄, WS₈ and WS₁₀ showcase the impact of wind-speed on the emis-



Table 1. An overview of the ADCHAM model setup in the BaseCase simulation and sensitivity runs.

Model Run	Details
BaseCase	T = 283 K, WS = 6 m/s, SST = 283 K, Rain = 10 mm/h, [DMS] = 10 nM, [NH _x] = 0.3 mmol/m ³
TEMP	Air temperature varied between 273K, 278K, 283K, 288K and 293K
WS	Wind-speed varied between 2 m/s, 4 m/s, 6 m/s, 8 m/s and 10 m/s
PRCP	Precipitation varied between 2.5 mm/h, 5 mm/h, 10 mm/h and 15 mm/h
SST	Sea surface temperature varied between 278 K, 283 K, 288 K and 293 K
DMS	Sea surface concentration of DMS varied between 5 nM, 10 nM, 15 nM and 20 nM
NH _x	Sea surface concentration of NH _x varied between 0.1 mmol/m ³ , 0.2 mmol/m ³ , 0.3 mmol/m ³ and 0.4 mmol/m ³
CLOUD	Mid-day and midnight clouds are introduced after the precipitation event
noMSIAabs	Removes the MSIA abstraction pathway by OH
noMSIAadd	Removes the MSIA addition pathway by OH
ΔCH ₃ SO ₂	Uses the thermal decomposition rate for CH ₃ SO ₂ from Jacob et al. (2024)
ΔCH ₃ SO ₃	Uses the thermal decomposition rate for CH ₃ SO ₃ from Cao et al. (2013)

sions of compounds to the model, especially emissions of DMS, NH₃ and sea-spray. These simulations represent conditions of
210 low, moderate and high wind-speed. PRCP_{2.5}, PRCP₅ and PRCP₁₅ show the impact of varying the amount of precipitation on
day two of the simulation. Here, precipitation at 2.5-5.0 mm/h is classified as moderate rain, while precipitation from 10-15
mm/h is classified as heavy rain. The sea surface concentration of DMS is varied from the concentration used in the BaseCase
simulation (10 nmol/L) to 5 nmol/L in [DMS]₅, 15 nmol/L in [DMS]₁₅ and 20 nmol/L in [DMS]₂₀. This represent con-
ditions ranging from weak to moderate and strong phytoplankton blooms. [NH_x]_{0.1}, [NH_x]_{0.2} and [NH_x]_{0.4} demonstrate the
215 effect of the sea surface concentration of total dissolved ammonium, which in turn impacts the emissions of NH₃ to the marine
atmosphere. NH_x concentrations of 0.2 mmol/m³ are representative of conditions in the North Atlantic Ocean between May
and July, where phytoplankton blooms are at their peak in the region. The same is true in the Southern Ocean during December
to February, where NH_x concentration of 0.4 mmol/m³ are common. In the BaseCase simulation, no clouds are introduced
in the model after the precipitation event at the end of day two. In the CLOUD sensitivity run, mid-day and mid-night clouds
220 continue to be present after the precipitation event to test the impact of clouds on NPF in the simulation.

In addition to the sensitivity runs focusing on emissions and different meteorological and hydrological conditions, certain
aspects of the DMS oxidation chemistry and its impact on DMS-derived NPF are also examined. In ΔCH₃SO₂, the rate for
the thermal decomposition of CH₃SO₂ from Jacob et al. (2024) is used as opposed to the rate from MCMv3.3.1, to test how
225 an increase in SO₂ at the expense of SA and MSA impacts NPF. In ΔCH₃SO₃, the rate from Cao et al. (2013) for the thermal
decomposition of CH₃SO₃ is used as opposed to the one from MCMv3.3.1 to demonstrate the impact from an increase in SA
from CH₃SO₃. In noMSIAabs and noMSIAadd, the reactions for the H-abstraction from MSIA by OH and OH addition to

MSIA are removed from the simulation. This is done to showcase the role of the MSIA compound in the formation and growth of aerosol particles from DMS. In addition to the results depicted in figures 1-4 from the main text, further figures can be found
230 in the SI, sections S1–S10.

2.4 Rate coefficients calculations

In this study, two key reactions on the oxidation of MSIA by OH were modified based on quantum chemical calculations. This was done due to their impact on SA and MSA production in the gas-phase (Wollesen de Jonge et al., 2021; Shen et al., 2022) and thus DMS-derived NPF in the MBL. The two reactions concern the H-abstraction from MSIA by OH and the
235 addition of OH to MSIA. Quantum chemical calculations were used on the following principles: [1] If the reaction coefficient had previously been based on estimates, then the quantum chemical calculations were used to obtain both the reaction rate and the temperature dependency for the reaction. [2] If the reaction coefficient has been determined experimentally but at a fixed temperature, then the quantum chemical calculations were used to obtain the temperature dependency for the reaction. In the context of this work, quantum chemical calculations were therefore used to obtain the temperature dependency for the
240 H-abstraction from MSIA by OH, since the rate of reaction had already been determined at a fixed temperature (298K) by Kukui et al. (2003). As no experimental rates exist for the addition of OH to MSIA, both the reaction rate and temperature dependency were calculated using quantum chemical calculations.

For the quantum chemical calculations, all geometry optimizations and harmonic vibrational frequency calculations of the
245 reactants, transition states (TS), intermediates (IM), and products were performed at the M06-2X/6-311+G(3df,2p) level of theory (Zhao and Truhlar, 2008). Intrinsic Reaction Coordinate (IRC) calculations at the same level were carried out to confirm that each TS connects the intended reactants and products. Single-point energy (SPE) calculations were performed at the ROHF-ROCCSD(T)-F12a/cc-pVDZ-F12 (hereafter denoted as F_{12a}) level (Adler et al., 2008), including zero-point energy corrections obtained at the M06-2X/6-311+G(3df,2p) level. This combination of methods has been widely applied to study the
250 transformations of peroxy and alkoxy radicals, and its accuracy is well established as a 'gold-standard' approach (Wang et al., 2020; D'Ambro et al., 2022; Møller et al., 2019). All quantum chemical calculations were performed using the Gaussian 16 and Molpro 2024.3 software packages (Frisch et al., 2016; Werner et al., 2020).

To account for the effects of multiple conformers of the reactants and transition states on the reaction mechanism, both single
255 and multi-conformer approaches were employed to balance computational cost and accuracy. Based on the single-conformer results, multi-conformer effects were explicitly considered for key reaction channels, including H-abstraction and OH-addition reactions of MSIA with OH, as well as the subsequent reactions of the addition intermediates (IM_{add}). Following previous work (Fu et al., 2022, 2024a, b), a conformational sampling scheme using Molclus and Gaussian 16 was adopted to explore the low-energy conformers of the relevant reactants and transition states. For kinetic analysis, the electronic energies were taken from
260 the F_{12a} calculations, while the partition functions were derived from the M06-2X/6-311+G(3df,2p) results. Rate constants were obtained using multiconformer transition state theory (MC-TST). One-dimensional unsymmetrical Eckart barriers were

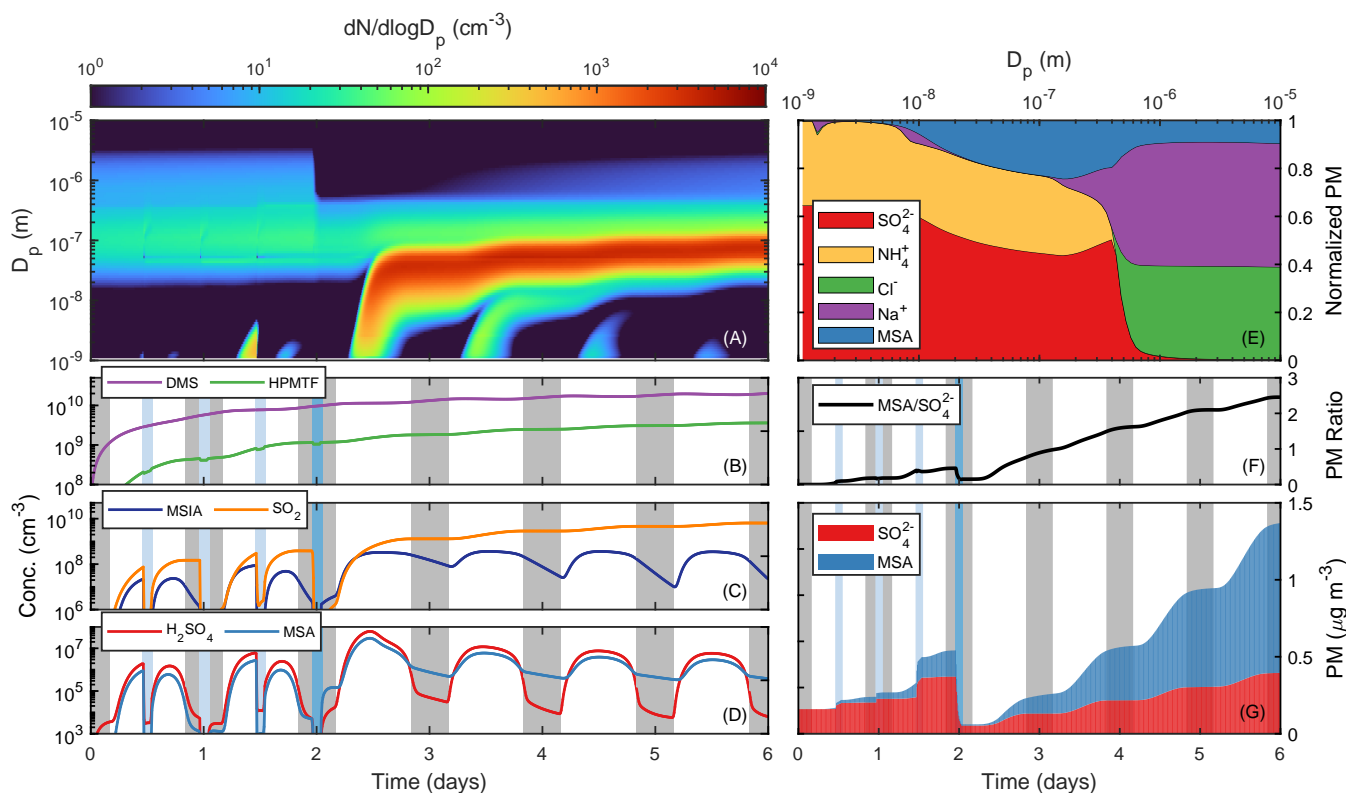


Figure 2. DMS driven NPF and growth in the pristine MBL. Panel (a) shows the particle number size distribution for the full simulation period, while panel (b), (c) and (d) show the gas-phase concentrations of DMS and HPMTF, MSIA and SO_2 along with SA and MSA, respectively. Panel (d) shows the normalized chemical composition for the full size distribution, panel (e) the $\text{MSA}/\text{SO}_4^{2-}$ PM ratio and panel (f) the SO_4^{2-} and MSA PM. The grey bars represent night-time conditions while the light and dark blue bars depict cloud and precipitation events, respectively. The results are obtained from the BaseCase simulation.

applied to account for quantum tunnelling in reactions involving H-shift or H-abstraction (Eckart, 1930). All rate constants were calculated with the KiSTheIP program (Canneaux et al., 2014). The calculations are discussed in more detail in the SI, Section S1.

265 3 Results and Discussion

3.1 DMS-derived NPF and growth

At the conditions given in the BaseCase model setup, a distinct NPF event takes place on the third day of the simulation following the precipitation event (Fig. 2a). The formation and growth of particles is driven by emissions of DMS, which enters the model at 8.3×10^9 molecules $\text{cm}^{-2} \text{s}^{-1}$ (6 m/s wind-speed) and gradually builds up to reach a concentration of 0.92 ppb at



270 the end of the simulation (Fig. 2b). As the simulation is initiated with high concentrations of sea spray aerosol particles ($18.6 \mu\text{g m}^{-3}$) and partial cloud cover, NPF is suppressed on day one and day two. The suppression of NPF is driven by the high SA condensation sink ($1.4 \times 10^{-3} \text{ s}^{-1}$ before the precipitation event) and the uptake of SA and SA precursors to the cloud droplets. These precursors include MSIA and SO_2 which partition to the cloud droplets during cloud cover (Fig. 2c) to form MSA and SO_4^{2-} , respectively. This means that MSIA and SO_2 are almost completely removed from the gas-phase during cloud cover.

275 Consequently, the mean SA gas-phase concentration is lower on day two of the simulation ($1.2 \times 10^6 \text{ cm}^{-3}$) compared to day three ($1.6 \times 10^7 \text{ cm}^{-3}$). The uptake and processing of water soluble species in the activated cloud droplets causes a small but distinct Hoppel minima to form in the size distribution during days 1-2 (Fig. 2a), driven predominantly by the uptake and aqueous-phase processing of DMSO, MSIA and SO_2 . The minima persists after the precipitation event and highlights the impact that aqueous-phase chemistry in cloud droplets has on the aerosol particle population over the ocean. MSA is also removed

280 during cloud cover, but since it possesses semi-volatile characteristics (Henry's law solubility of $6.7 \times 10^8 \text{ mol kg}^{-1} \text{ atm}^{-1}$ at 283K) a fraction of it will evaporate back to gas-phase after each cloud period (Fig. 2d). During the cloud free conditions representative of days 3-6, MSA follows a similar diurnal trend as SA with peak production and concentration during midday and lower concentrations at night. HPMTF builds up in the gas-phase in the same way as DMS, reaching a concentration of 166 ppt at the end of the simulation (Fig. 2b).

285

On day three of the simulation, the precipitation event removes a considerable fraction of the aerosol PM, thereby decreasing the condensation sink to $1.1 \times 10^{-4} \text{ s}^{-1}$. This spurs an increase in the SA gas-phase concentrations which causes SA and NH_3 to cluster and form new particles. The continues condensation of SA and NH_3 ensures that the newly formed clusters grow, first into a distinct nucleation mode and thereafter into the Aitken mode which reaches a mode particle diameter of 73 nm

290 (25th-75th prct.: 60-88 nm) at the end of the simulation. Additional NPF on days 4-6 is suppressed due to the increase in the condensation sink from the additional sea-spray PM and the particles formed in the NPF event on day three. The gas-phase concentration of MSIA, MSA and SA decreases correspondingly as they are lost to the increasing concentration of said particles (Fig. 2c and 2d). SO_2 , on the other hand, accumulates in the gas-phase during days 3-6 as the lack of clouds prevents it from partitioning efficiently to the particle-phase. This also means that the SA source flux from SO_2 increases towards the

295 end of the simulation whereas the SA source flux from CH_3SO_3 decreases in correspondence with the decrease in MSIA (Fig. S6). Consequently, SO_2 comprises 21% of the SA source flux during day six compared to 3% during day three. As a result, SO_2 becomes less important for the initial NPF as the conversion of SO_2 to SA is considerably slower than the conversion of CH_3SO_3 to SA. When SO_2 finally reaches a concentration where it contributes significantly to the production of SA, the sea-spray and DMS-derived PM concentration has become too high for new particles to form efficiently. Nucleation rates for

300 the SA- NH_3 system obtained with the RI-CC2 method are significantly higher than those obtained with the DLPNO method (maximum nucleation rate of $2.0 \text{ cm}^{-3}\text{s}^{-1}$ on day three of the simulation using RI-CC2 as opposed to $0.13 \text{ cm}^{-3}\text{s}^{-1}$ when using DLPNO)(Fig. S12). This rate leads to a 2.2 times increase in the total PN concentration at the end of the simulation. The increase in the PN concentration stunts the growth of the particles as more SA is needed to grow said particles into the nucleation and Aitken mode. As a result, the growth mode only reaches a mode particle diameter of 56 nm (25th-75th prct.:



305 46-68 nm) at the end of the simulation. Consequently, using the RI-CC2 method as opposed to the DLPNO method to obtain nucleation rate for the SA-NH₃ system will increase the total number of particles but decrease the number of particles that may reach the CCN size range.

SO₄²⁻ and NH₄⁺ PM dominates the chemical composition of the aerosol particles formed during the NPF event and in the subsequent growth mode (Fig. 2e). This is caused by the ability of SA to condense irreversibly to the particle-phase, with NH₃ aiding the growth by neutralizing the otherwise acidic aerosol particles. According to ADCHAM, DMS-derived SA and natural emissions of NH₃ from the surface ocean are capable of sustaining the growth of newly formed aerosol particles into the nucleation and Aitken mode. MSA does not contribute significantly to the growth of the smaller particles, as its semi-volatile characteristics mainly allows it to condense on the larger sea-spray particles. MSA PM nevertheless aids the growth of the particles in the Aitken and upper end of the nucleation mode, with particularly high PM concentrations in the accumulation and coarse mode particles (Fig 2e). This happens as 85% of MSA is formed in the aqueous-phase of the deliquesced aerosol particles and cloud droplets from the oxidation of dissolved and dissociated MSIA by O₃. The remaining MSA production happens in the gas-phase through the addition of OH to MSIA (8%) and from the reaction of CH₃SO₃ with HO₂ (6%) and DMS (2%). While MSA formed in the gas-phase is able to condense on particles in the nucleation and Aitken mode size range, MSIA mainly partitions to the coarse mode deliquesced sea-spray particles where it is converted to MSA. This tendency is evident from the decrease in the MSA PM during the precipitation event. Here, the MSA PM decreases by 95% as opposed to 86% for the SO₄²⁻ PM as the coarse mode particles containing most of the MSA PM are removed more efficiently through wet-deposition than particles in the lower size ranges (Fig. 2g). After the precipitation event, the MSA PM increases disproportionately to the SO₄²⁻ PM as the lack of clouds prevents SO₂ from being converted to SO₄²⁻. As MSA continues to be produced in the deliquesced sea spray particles, the MSA/SO₄²⁻ PM ratio increases throughout the simulation from an average ratio of 0.3 on day three to 2.3 on day six (Fig. 2f).

3.2 Impact of metrological and hydrological conditions

3.2.1 Air temperature

The air temperature within the MBL dictates different aspects that influences the formation and growth of aerosol particles. This includes the gas-phase and aqueous-phase chemistry, the rate of molecular clustering and evaporation, the condensation of low volatile species to the particles and the uptake of water-soluble species to deliquesced particles and cloud droplets. The air temperature therefore constitutes an important factor in NPF and particle growth.

A fundamental role of the air temperature is its ability to control the amount of water that the air can hold. Warmer air holds more water than cold air and as a consequence produces higher concentrations of OH, with a mean concentration throughout the simulation of $5.2 \times 10^5 \text{ cm}^{-3}$ in TEMP₂₉₃ compared to $1.8 \times 10^5 \text{ cm}^{-3}$ in TEMP₂₇₃. Higher concentrations of OH also leads to higher concentrations of HO₂, which promotes the production of HOX (X = Cl, Br, I) which catalytically activates the halogen species ICl, BrCl and Cl₂ from the sea spray particles and thus promotes the concentration of halogen oxidants in the

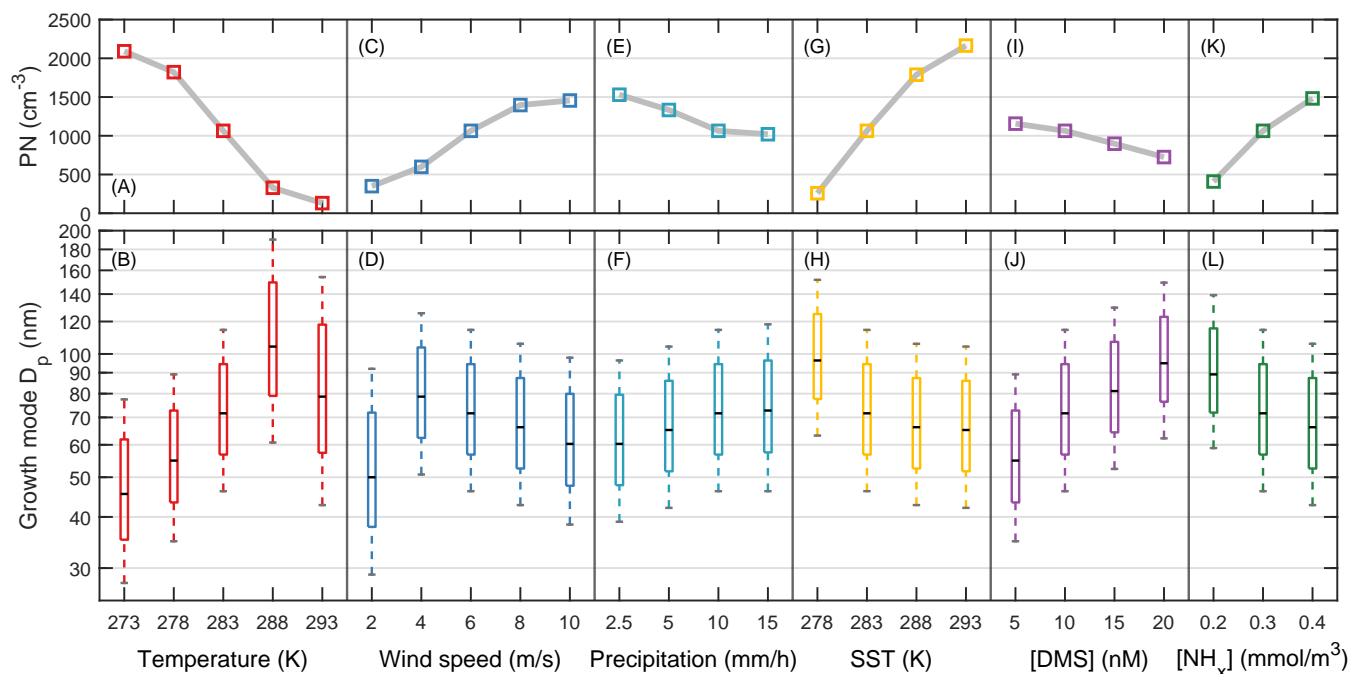


Figure 3. DMS-derived growth mode in the pristine MBL. Depicts the aerosol growth mode particle size distribution and total PN concentration at the end of the simulation for (a-b) varying temperatures, (c-d) varying wind-speeds, (e-f) varying rates of precipitation, (g-h) varying sea surface temperatures, (i-j) varying surface ocean concentrations of DMS and (k-l) varying surface ocean concentrations of total dissolved NH_x . The box plots represents the 5th, 25th, 75th and 95th percentile of the growth mode and the black line represents the mode particle diameter. Simulations where no NPF event took place are not included in the figure.

gas-phase (Brauer et al., 2013). The oxidative capacity of the MBL therefore increases with temperature, which is seen in the mean DMS sink flux throughout the simulation which increases from $4.1 \times 10^4 \text{ cm}^{-3}\text{s}^{-1}$ in TEMP_{273} to $4.9 \times 10^4 \text{ cm}^{-3}\text{s}^{-1}$ in TEMP_{293} (Fig. S16). At the same time, temperature also dictates the ratio of the DMS abstraction pathway to the DMS addition pathway, as OH addition to DMS is favoured at lower temperatures ($k_{\text{DMS,abs}}/k_{\text{DMS,add}} = 0.5$ at 273 K and 1 atm compared to 1.6 at 293 K). The temperature driven branching of the OH-initiated oxidation of DMS propagates through the mechanism and dictates the production of species in both the abstraction and addition pathway. As a result, the mean source flux of DMSO and MSIA in the addition pathway is higher in TEMP_{273} ($2.4 \times 10^4 \text{ cm}^{-3}\text{s}^{-1}$ and $1.9 \times 10^4 \text{ cm}^{-3}\text{s}^{-1}$, respectively) compared to TEMP_{293} ($1.6 \times 10^4 \text{ cm}^{-3}\text{s}^{-1}$ and $1.4 \times 10^4 \text{ cm}^{-3}\text{s}^{-1}$, respectively) in spite of higher OH concentrations in TEMP_{293} (Fig. S20). The temperature dependency on the initial oxidation of DMS is amplified by the addition of BrO to DMS forming DMSO, which is favoured at lower temperatures. Although cold conditions promotes the production of DMSO and MSIA, the fraction that oxidizes to form CH_3SO_2 , CH_3SO_3 and ultimately SA and MSA in the gas-phase is limited by the uptake of MSIA to the deliquesced aerosol particles. The mean sink flux of MSIA to the deliquesced particles is 4.0 times higher at 273 K compared to 293 K, whereas the sink flux of MSIA through H-abstraction by OH is 3.0 times higher at 293 K



compared to 273 K. Consequently, colder temperatures promotes the uptake of MSIA to the aqueous-phase whereas warmer temperatures promotes the continues oxidation of MSIA in the gas-phase. The effect is evident from the $\text{MSA}/\text{SO}_4^{2-}$ PM ratio (7.0 in TEMP_{273} and 0.9 in TEMP_{293}) as the uptake of MSIA to the deliquesced aerosol particles promotes the production of MSA through aqueous-phase oxidation by O_3 .

355

The continues production of CH_3SO_2 originates both from the oxidation of MSIA by OH in the addition pathway and through the propagation of species in the abstraction pathway. However, due to the low NO_x conditions in the simulation (representative of the pristine MBL), the NO_x driven oxidation of CH_3SO and CH_3SOO_2 in the abstraction pathway make up < 1% of the CH_3SO_2 source flux throughout all temperature sensitivity runs. The isomerization of CH_3SOO comprises the only significant source of CH_3SO_2 from the abstraction pathway, making up 4% of the CH_3SO_2 source flux in the BaseCase simulation (Fig. S10). The oxidation of MSIA by OH, on the other hand, makes up 96% of the CH_3SO_2 source flux. It is evident therefore that the oxidation of species in the addition pathway dictates the production of CH_3SO_2 , CH_3SO_3 and thus direct SA and MSA production in the gas-phase.

360

365

While the production of CH_3SO_2 continues to increase with temperature, its oxidation by O_3 to form CH_3SO_3 is impacted by the thermal decomposition of CH_3SO_2 into CH_3OO and SO_2 (Figure 1). Said decomposition increases with temperature, causing the $F_{\text{CH}_3\text{SO}_2, \Delta}/F_{\text{CH}_3\text{SO}_2 + \text{O}_3}$ sink flux ratio to increase from 0.1 in TEMP_{273} to 1.3 in TEMP_{293} . As a consequence, the CH_3SO_3 production stagnates as the temperature increases from 273 K to 283 K and starts to drop as the temperature exceeds 283 K (Fig. S22). This directly impacts the production of SA which follows the trend of CH_3SO_3 through the thermal decomposition of CH_3SO_3 into CH_3OO , SO_3 and thus SA. As the simulation progresses and additional sea-spray enters the MBL, the temperature effect on the uptake of MSIA to the sea-spray becomes increasingly important for the production of SA. Following the precipitation event on day three, sea-spray concentrations remain relatively low. This in combination with higher concentrations of DMSO ensures that the concentration of MSIA on day three is higher in TEMP_{273} compared to TEMP_{293} . On day four-six, however, MSIA concentrations in TEMP_{273} falls bellow that in TEMP_{293} as the colder temperatures ensures that MSIA partitions efficiently to the aqueous-phase. As a result, the CH_3SO_2 , CH_3SO_3 and SA source flux decreases from day three to day six in TEMP_{273} but increases during the same time in TEMP_{293} , both following the continues increase in the DMS concentration (Fig. S17, S21 and S22).

370

375

380

In addition to the effect of temperature on the uptake of MSIA to the deliquesced particles, SA production from SO_2 also becomes increasingly important with the increase in temperature. The SO_2 source flux increases by a factor of 3.8 between 273 K and 293 K, mainly driven by the increase in HPMTF production but also from the thermal decomposition of CH_3SO_2 which makes up 17% of the SO_2 source flux in TEMP_{293} as opposed to 4% in TEMP_{273} (Fig. S19). The formation of HPMTF is favoured at higher temperatures as the OH addition to DMS becomes less favourable, thereby promoting the abstraction pathway and thus the autoxidation of $\text{CH}_3\text{SCH}_2\text{O}_2$ into HPMTF and ultimately SO_2 . Furthermore, the autoxidation itself becomes faster as the temperature increases as the internal H-abstractions by the peroxy radicals in $\text{CH}_3\text{SCH}_2\text{O}_2$ and

385



OOCH₂SCH₂OOH are favoured at higher temperatures. SO₂ therefore reaches a concentration of 519 ppt in TEMP₂₉₃ as opposed to 130 ppt in TEMP₂₇₃, thereby comprising 27% and 7% of the total SA source flux throughout the simulations, respectively. The combination of the decrease in the uptake of MSIA to the sea-spray particles and the increase in the production of SO₂ means that the total SA source flux increases from 273 K to 288 K (Fig. S17). Beyond 288 K, however, the thermal decomposition of CH₃SO₂ limits the oxidation of CH₃SO₂ by O₃ to a degree where the production of CH₃SO₃ and thus SA starts to decrease. Consequently, the total SA source flux throughout the simulation decreases as the temperature exceeds 288 K.

MSA production in the gas-phase remains relatively stable across the temperature interval, although its source varies. At 273 K, H-abstraction from DMS by CH₃SO₃ and the reaction of HO₂ with CH₃SO₃ makes up 27% and 46% of the MSA gas-phase source flux, respectively. At 293 K, OH addition to MSIA dominates the production of MSA comprising 80% of the MSA gas-phase source flux. The difference comes down to the decrease in MSIA partitioning to the deliquesced particles and higher OH concentrations in warm conditions, which promotes the addition of OH to MSIA despite the inverse relationship between temperature and the addition reaction rate itself. In cold conditions, DMS concentrations are higher due to the limited oxidation capacity of the atmosphere and CH₃SO₃ is less likely to undergo thermal decomposition thereby promoting the production of MSA via H-abstraction from DMS by CH₃SO₃.

In addition to the impact of temperature on the chemistry and uptake of water soluble species to the aqueous-phase, temperature also impacts the rate by which the initial clusters form and grow. Here, the maximum SA-NH₃ derived nucleation rate on day three of the simulation following the precipitation event increases as the temperature decreases from 0.3 × 10⁻² cm⁻³s⁻¹ at 293 K to 0.9 cm⁻³s⁻¹ at 273 K (Fig. S15). The difference is driven predominantly by the temperature effect on the cluster stability as the NH₃ and SA concentrations increases with increasing temperatures. The higher nucleation rate at 273 K promotes the total PN concentration, which was found to be 15 times higher at the end of the simulation in TEMP₂₇₃ compared to TEMP₂₉₃ (Fig. 3a).

The continues growth of the particles changes throughout the simulation. During day one-two, the particle growth is dictated by the uptake and complete removal of water soluble gas-phase species to the cloud droplets. In terms of the MSA PM, the impact of clouds is less pronounced as MSIA already partitions efficiently to the deliquesced particles during cloud-free periods. Clouds nevertheless promotes the production of SO₄²⁻ PM through the uptake and aqueous-phase processing of SO₂. Consequently, the SO₄²⁻ PM increases linearly with the temperature during days one-two. During the remainder of the simulation, however, the total SA source flux and thus the production of SO₄²⁻ PM increases from 273 K to 288 K but decreases from 288 K to 293 K. This happens as the production of CH₃SO₃ and in turn SA stagnates and starts to decrease beyond 288 K as the fraction of CH₃SO₂ that decomposes into SO₂ becomes higher. If left to run for an extended period, the total SA source flux in TEMP₂₉₃ would eventually surpass that of those in the remaining simulations due to the increase in the production of SA from SO₂. However, as the production of SA from CH₃SO₃ dictates the production of the new particles following the precipitation event, the particles formed at 293 K would not reach the size of those produced at 288 K. As a



result, the DMS-derived particles reach their maximum mode diameter of 106 nm (25th-75th prct.: 85-136 nm) at 288 K, with the particles reaching only 46 nm (25th-75th prct.: 38-57 nm) at 273 K and 81 nm (25th-75th prct.: 62-106 nm) at 293 K (Fig. 3b). The DMS-derived NPF and growth therefore does not change linearly with temperature, but peaks around moderate temperature conditions. At higher temperatures, the SA production is limited by the thermal decomposition of CH_3SO_2 which
425 limits the production of CH_3SO_3 and thus SA. At lower temperatures, the SA production is limited by the uptake of MSIA to the deliquesced particles, which decreases the production of CH_3SO_2 , CH_3SO_3 and thus SA. It should be noted that the high nucleation rate at the lower temperatures also lowers the growth of the particles, as more SA is needed to grow the high concentration of newly formed particles into the nucleation and Aitken mode.

3.2.2 Wind-speed

430 The wind-speed adjacent to the sea surface makes up the most important metrological factor in the emission of gases and sea spray particles from the ocean to the MBL. The correlation between the gas-flux and the wind-speed 10 meters above the sea surface (U_{10}) may be linear (Liss and Merlivat, 1986), super-linear (Blomquist et al., 2017) ($F \propto U_{10}^{1.33}$) or quadratic (Wanninkhof, 2014; Nightingale et al., 2000) depending on the study that is used to calculate the transfer velocity k_w . Well established emission databases such as the Copernicus Atmosphere Monitoring Service (CAMS) relies on the quadratic trans-
435 fer velocity from Nightingale et al. (2000) to calculate the sea-air flux of DMS, despite the fact that the relationship between the transfer velocity and wind-speed from said study has not been determined specifically for DMS. In this work we utilize the super-linear transfer velocity from Blomquist et al. (2017), as it was calculated specifically for DMS. As a consequence, the DMS flux and atmospheric DMS-derived concentrations reported here are smaller than those in model studies that rely on emissions from CAMS or utilize a quadratic transfer velocity to calculate the flux of DMS in their model, especially during
440 conditions with high wind-speed. Emissions decrease further if using the linear transfer velocity from Liss and Merlivat (1986). For sea spray, the current parameterizations generally agree on using an empirical power law fit for the sea spray flux as a function of wind-speed ($F \propto U_{10}^{3.41}$) (Sofiev et al., 2011; Salter et al., 2015). Concentrations of sea spray in the MBL consequently depends heavily on wind-speed, with much higher emissions during strong winds compared to calm conditions.

445 In the sensitivity runs WS_2 , WS_4 , WS_8 and WS_{10} , the wind-speed in the simulation is varied from 2 m/s to 10 m/s in addition to the 6 m/s used in the BaseCase simulation. DMS emissions vary by close to an order of magnitude across this wind-speed interval, ranging from 1.9×10^9 molecules $\text{cm}^{-2} \text{s}^{-1}$ at 2 m/s to 1.6×10^{10} molecules $\text{cm}^{-2} \text{s}^{-1}$ at 10 m/s. The DMS concentrations consequently reaches 229 ppt in WS_2 and 808 ppt in WS_{10} (Fig. S23). Higher concentrations of DMS are seen in BaseCase (922 ppt) and WS_8 (1089 ppt), as the substantial sea spray particle concentrations in WS_{10} ($65 \mu\text{g}/\text{m}^3$ at the end
450 of the simulation as opposed to $0.3 \mu\text{g}/\text{m}^3$ in WS_2) ensures higher concentrations of halogen oxidants BrO and Cl and thus a higher DMS sink flux than in the remaining simulations (Fig. S26). The increase in DMS emissions and the oxidative capacity of the MBL also ensures that the secondary aerosol PM increases in accordance with the wind-speed ($0.2 \mu\text{g}/\text{m}^3$ in WS_2 and $6.0 \mu\text{g}/\text{m}^3$ in WS_{10}). Strong winds favour the production of MSA as opposed to SO_4^{2-} , as the increase in sea spray increases the uptake of MSIA to the deliquesced aerosol particles and thus promotes the aqueous-phase production of MSA. As a result,



455 the $\text{MSA}/\text{SO}_4^{2-}$ PM ratio is 0.5 in WS_2 and 8.3 in WS_{10} .

The formation and growth of DMS derived particles in the MBL at different wind-speeds is dictated by the emissions of DMS, NH_3 and sea spray. In WS_2 , sea spray emissions and thus the condensation sink remains low ($0.6 \times 10^{-3} \text{ s}^{-1}$ at the end of the simulation as opposed to $4.6 \times 10^{-3} \text{ s}^{-1}$ in WS_{10}). The low condensation sink allows DMS-derived SA and NH_3 to form and
460 grow particles during days 3-6 in the simulation (Fig. S24), although the maximum nucleation rate during these days remains moderately low at $1.5 \times 10^{-2} \text{ cm}^{-3} \text{ s}^{-1}$. New particles are able to form on day six in WS_2 as the sea spray concentration builds up slowly, thus keeping the condensation sink low. Nucleation and growth rates in WS_2 remain low compared to the other simulations, as the low wind-speed also limits the emissions of DMS and NH_3 . The opposite is true in WS_{10} , where emissions of DMS and NH_3 are high but the growth is limited by the high concentration of sea spray. As a results, new particles are able to
465 form relatively efficiently on day three (following the precipitation event) when sea spray concentrations have not yet reached a level where they efficiently suppress NPF. On day four to six, however, the increasing condensation sink (both from the sea spray and from the DMS-derived growth event) prevents any new particles from forming. As the high condensation sink in WS_{10} also limits the growth of the newly formed particles, said particles only reach a mode particle diameter of 61 nm (25th-75th prct.: 51-74 nm) at the end of the simulation (Fig. 3d). In WS_2 , the particles reach a mode diameter of 52 nm (25th-75th
470 prct.: 41-65 nm). These two scenarios illustrate that an optimal wind-speed exists where the condensation sink is sufficiently low and the concentration of precursor gases sufficiently high for particles to grow. Here, we demonstrate that the overall growth of the particles peaks in WS_4 at a mode diameter of 80 nm (25th-75th prct.: 66-96 nm). The total PN concentration, however, increases in according with the wind-speed from $4.1 \times 10^2 \text{ cm}^{-3}$ in WS_2 to $1.5 \times 10^3 \text{ cm}^{-3}$ in WS_{10} (Fig. 3c). In conclusion, moderate wind-speeds (4-6 m/s) comprises the optimal conditions for DMS-derived particles to grow within the
475 MBL. During conditions of light winds, the growth of the new particles is limited by the lack DMS and NH_3 . During strong winds, the growth is limited by the high condensation sink caused by the sea spray emissions. As the concentration of sea spray particles remains low on day three of the simulation following the precipitation event in WS_{2-10} , the rate of nucleation and thus the total PN concentration increases in accordance with the wind-speed due to higher emissions of DMS and NH_3 .

3.2.3 Precipitation

480 Over the open ocean, precipitation is essential for the formation of new particles as it efficiently lowers the concentration of accumulation and coarse mode particles. The decrease in particle surface area lowers the condensation sink and allows SA to reach higher concentrations in the gas-phase. In the BaseCase simulation, a heavy rainfall of 10 mm/h is introduced to the model for one hour during the night-time cloud event between day two and day three. This rainfall efficiently lowers the sea spray PM concentration by 99% which causes the mean SA gas-phase concentration to increase by an order of magnitude
485 (factor 12.3) on day three compared to day two. The increase in the gas-phase concentrations of SA subsequently sparks a distinct NPF event on day three. In the $\text{PRCP}_{2.5}$ and PRCP_5 sensitivity runs, representing conditions of moderate precipitation, the growth mode on day three remains present in the simulation despite lower concentrations of SA (Fig. S34). This happens as these precipitation rates still remove 89% and 96%, respectively, of the available sea-spray PM. At 2.5 mm/h precipitation, the



growth rate of the NPF event on day three was found to be 2.8 nm/h compared to 3.3 nm/h at 5 mm/h precipitation and 4.0
490 nm/h at 10 mm/h precipitation. The newly formed particles continue to grow and reach a mode diameter of 61 nm (25th-75th
prct.: 51-74 nm), 66 nm (25th-75th prct.: 55-80 nm) and 73 nm (25th-75th prct.: 60-88 nm) towards the end of the simulation in
PRCP_{2.5}, PRCP₅ and BaseCase, respectively (Fig. 3f). Our results, therefore, indicate that new particles formed over the ocean
can reach the Aitken mode size range within a couple of days, even at moderate rates of precipitation. Precipitation beyond 10
mm/h has less impact on the NPF and growth since the far majority of the coarse mode sea spray particles has already been
495 removed at this precipitation rate. As a consequence, the growth rate on day three of the simulation in PRCP₁₅ increases to just
4.3 nm/h with the newly formed particles reaching a mode diameter of 74 nm (25th-75th prct.: 61-89 nm) at the end of the
simulation. The total PN concentration at the end of the simulation is higher in PRCP_{2.5} compared to PRCP₁₀ (Fig. 3e), as less
of the NH₄⁺ PM has been removed from the atmosphere. As a result, more NH₃ evaporates back into the gas-phase following
the precipitation event which helps to drive the initial NPF. The continues growth of these particles are nevertheless stunted by
500 the decreased production of SA in the gas-phase.

3.2.4 Sea surface temperature

All marine emissions, be it sea spray particles or gases, depend on the sea surface temperature. For gases, the sea to air flux is
generally calculated as the product between the gas exchange coefficient k and the concentration gradient between the air-sea
interface (Eq. 1) (Ziska et al., 2013).

$$505 \quad F = k(C_w - C_a H^{-1}) \quad (1)$$

Here, C_w is the concentration of the gas in water, C_a is the concentration of the gas in air and H is the dimensionless Henry's law
solubility. The gas exchange coefficient depends both on the wind-speed and the sea surface temperature through the Schmidt
number for each gas. The Schmidt number, which prescribes the ratio of the kinematic viscosity of water to the diffusivity
of a specific gas in water, decreases for increasing sea surface temperatures as water becomes less viscous and gases diffuse
510 easier in warmer waters. From the inverse relationship between the gas exchange coefficient and the Schmidt number it follows
that higher sea surface temperatures increases the rate by which the gas leaves the surface ocean. In addition, the Henrys law
solubility dictates that gases are less soluble in warm as opposed to cold water, thereby increasing the concentration gradient
between the air-sea interface in warmer waters.

515 For the emission flux of sea spray particles, the sea surface temperature impacts both the size of the particles emitted as well
as total emitted PM. While uncertain, it is currently believed that the emission rate of smaller particles is favoured at low
temperature as opposed to the emission rate of larger particles which is favoured at higher temperatures (Barthel et al., 2019).
While the emitted particles are smaller in cold waters the number of emitted particles tend to be higher than in warm waters.
Overall, this leads to less PM but higher PN when the sea surface temperature is low as opposed to higher PM but lower PN



520 when the sea surface temperature is high.

The SST₂₇₈, SST₂₈₈ and SST₂₉₃ sensitivity runs demonstrate how the emissions of gases and sea spray PM increases with increasing sea surface temperature. Comparing results from the SST₂₇₈ and SST₂₉₃ sensitivity runs, the emission of NH₃ increases by a factor of 4.9 while the emissions of DMS increases by 50%. Sea spray emissions increase as well, reaching a concentration of 9.3 μg/m³ and 15.9 μg/m³ at the end of the simulation in SST₂₇₈ and SST₂₉₃, respectively (Fig. S45). The effects of the emission increase across all the mentioned species are twofold. First, the overall production of secondary aerosol PM increases from 1.1 μg/m³ in SST₂₇₈ to 2.1 μg/m³ in SST₂₉₃, following the higher emissions of DMS which promotes the production of SO₄²⁻ and MSA PM. Second, the MSA/SO₄²⁻ PM ratio increases correspondingly from 2.0 to 3.4 as the production of MSA PM is favoured to the production of SO₄²⁻ PM due to the higher uptake of MSIA to the higher concentration of deliquesced sea spray particles. The uptake of MSIA to said particles constitutes 56% of the MSIA sink flux in SST₂₇₈ and 69 % in SST₂₉₃. The increase in DMS emissions with the increase in SST nevertheless outweighs the increase in the uptake of MSIA to the sea spray particles, ensuring that the SA production in the gas-phase becomes 33% higher in SST₂₉₃ compared to SST₂₇₈ (Fig. S47). The increase in the SA production along with the increase in NH₃ emissions also ensures that the maximum nucleation rate on day three of the simulation increases with the increase in SST, from 2.0×10⁻² cm⁻³s⁻¹ in SST₂₇₈ to 0.8 cm⁻³s⁻¹ in SST₂₉₃ resulting in the total PN concentration being 8.3 times higher in SST₂₉₃ compared to SST₂₇₈ (Fig. 3g). In conclusion, higher SST promotes DMS-derived NPF through an increase in the emissions of NH₃ and DMS and thus the production of SA. At the same time, said processes are suppressed by the increase in the sea spray PM concentration which promotes the uptake of MSIA and SA to the particle-phase. At the same time, the high concentration of new particles formed in SST₂₉₃ stagnates the growth of said particles as more SA is needed to grow the particles into the nucleation and Aitken mode. In SST₂₇₈, where significantly less particles are able to form, the particles are able to grow into larger sizes. As a result, the newly formed particles in SST₂₉₃ reach a particle mode diameter of 66 nm (25th-75th prct.: 54-80 nm) at the end of the simulation as opposed to 98 nm (25th-75th prct.: 82-116 nm) in SST₂₇₈ (Fig. 3h). It should be noted that strong blooms of phytoplankton are generally found in colder waters where nutrients are more readily available. As a consequence, warmer waters tend to have lower sea surface concentrations of DMS and NH_x (Lana et al., 2011; Hulswar et al., 2022; Paulot et al., 2015).

3.2.5 DMS surface ocean concentration

The concentration of DMS in the surface ocean varies globally in accordance with the presence of phytoplankton. These plankton species in turn depend on external factors such as nutrient availability and sunlight, resulting in substantial spatial and temporal variations in plankton blooms, and consequently in the surface ocean DMS concentration. In [DMS]₅, BaseCase, [DMS]₁₅ and [DMS]₂₀, we demonstrate the impact that low, moderate, and high concentrations of DMS may have on the DMS-derived NPF and growth within in the MBL. It should be noted that the concentration of DMS may reach even higher concentrations in nutrient rich waters near certain coastlines (Lana et al., 2011; Hulswar et al., 2022). The concentrations ap-



plied here are nevertheless representative of the pristine MBL governed by natural nutrient availability.

555 Unsurprisingly, higher surface ocean concentrations of DMS leads to higher gas-phase concentrations of DMS and thereby
DMS-derived secondary aerosol PM in the MBL. The impact on the chemistry, NPF and particle growth, however, is found
to be sub-linear. At a surface ocean concentration of 5 nM, DMS enters the MBL at 0.4×10^{10} molecules $\text{cm}^{-2} \text{s}^{-1}$ and
reaches a gas-phase concentration of 427 ppt at the end of the simulation. At 20 nM, the sea-air flux increases to 1.7×10^{10}
molecules $\text{cm}^{-2} \text{s}^{-1}$ and the concentration reaches 2.1 ppb. The ensuing processing of DMS and its reaction intermediates
560 and products changes in accordance with the availability of oxidant species. The source flux of halogen radicals remains rel-
atively unchanged following the increase in DMS concentrations from $[\text{DMS}]_5$ to $[\text{DMS}]_{20}$. The concentrations of OH and
 O_3 , however, are found to decrease as the DMS concentration increases (Fig. S53). On the final day of the simulation, the
mean OH and O_3 concentrations are 24% and 3% lower, respectively, in $[\text{DMS}]_{20}$ compared to $[\text{DMS}]_5$. As a result, the DMS
concentration in the gas-phase stagnates and becomes relatively stable as the simulation progresses in $[\text{DMS}]_5$ and BaseCase
565 as opposed to $[\text{DMS}]_{15}$ and $[\text{DMS}]_{20}$ where it accumulates. While the concentration of DMS-derived oxidation products in-
creases in accordance with the increase in DMS emissions, said increase stagnates as the DMS loading becomes higher. For
instance, a power law fit for the source flux of SO_2 , MSA and SA to the sea surface DMS concentration shows a sublinear
response for all species, with scaling exponents of 0.81, 0.92, and 0.66, respectively. The incremental increase in the MSA
source flux drops disproportionately to the other species as the production of MSA through the H-abstraction from DMS by
570 CH_3SO_3 increases with the concentration of DMS. Said reaction therefore makes up 7% of the MSA gas-phase source flux in
 $[\text{DMS}]_5$ as opposed to 25% in $[\text{DMS}]_{20}$. The increase in MSA happens at the expense of SA production, as CH_3SO_3 is less
likely to undergo thermal decomposition into SO_3 and thus SA.

The rate of particle formation on day three of the simulation is governed by the production of SA and the uptake of NH_3
575 to the particle phase. As the simulation progresses, the higher DMS loading acidifies the particles (2.1 and 1.2 mean bulk
particle-phase pH during days three-six in $[\text{DMS}]_5$ and $[\text{DMS}]_{20}$, respectively) thereby driving NH_3 into the aqueous-phase
(Fig. S55). This effect is most pronounced towards the end of the simulation, but even on day three the concentration of
 NH_3 is 67% lower in DMS_{20} compared to DMS_5 . The source flux of SA and thus the SA gas-phase concentration, however,
continues to increase with higher sea surface concentrations of DMS (Fig. S57). Still, the nucleation rate on day of three of the
580 simulation peaks at $0.15 \text{ cm}^{-3} \text{ s}^{-1}$ in $[\text{DMS}]_5$ and decreases to $0.10 \text{ cm}^{-3} \text{ s}^{-1}$ in $[\text{DMS}]_{20}$. The nucleation rate also impacts
the total PN concentration in the Aitken mode, which decreases from $[\text{DMS}]_5$ to $[\text{DMS}]_{20}$ (Fig. 3i). As the continues growth
of the particles relies mainly on the availability of SA in the gas-phase, the growth rate on day three of the simulation peaks in
 $[\text{DMS}]_{20}$ at 6.2 nm/h, compared to 2.8 nm/h in $[\text{DMS}]_5$. The same is true for the particle growth during the remainder of the
simulation, where the particles reach a mode diameter of 96 nm (25th-75th prct.: 81-114 nm) in $[\text{DMS}]_{20}$ compared to 56 nm
585 (25th-75th prct.: 46-89 nm) in $[\text{DMS}]_5$ (Fig. 3j). In conclusion, natural emissions of DMS during moderate to high sea surface
concentrations of DMS are able to form and grow aerosol particles that reach into the upper Aitken and accumulation mode
particle size range with the potential to act as CCN in the pristine MBL.



3.2.6 NH_x surface ocean concentration

It is well documented that the ocean can constitute a source of NH_3 to the atmosphere from dissolved NH_x in the surface ocean (Johnson et al., 2008; Paulot et al., 2020). This is particularly true at high latitudes in highly productive regions of the oceans with intense biological recycling of nitrogen. These same regions also experience the highest occurrence of phytoplankton blooms. Once in the atmosphere, NH_3 aids the SA- NH_3 clustering and therefore constitutes one of the most important precursors that drives NPF in the MBL. In addition, NH_3 helps to neutralize the otherwise acidic marine aerosol particles, ensuring that less acidic and more volatile species such as MSIA and MSA are able to partition to and dissociate in the aqueous-phase.

595

In $[\text{NH}_x]_{0.1}$, $[\text{NH}_x]_{0.2}$, BaseCase and $[\text{NH}_x]_{0.4}$ we perform simulations with low (0.1 mmol/m^3), moderate ($0.2\text{-}0.3 \text{ mmol/m}^3$) and high (0.4 mmol/m^3) concentrations of dissolved NH_x in the surface ocean. Higher concentrations of NH_x naturally leads to a higher emissions of NH_3 , with the NH_3 sea-air flux being 3.7 times higher in $[\text{NH}_x]_{0.4}$ compared to $[\text{NH}_x]_{0.1}$. The increase is sub-linear as the flux is regulated based on the concentration of NH_3 in the atmosphere. Once in the air, NH_3 helps to increase the pH of the predominantly acidic marine particles from 1.4 in $[\text{NH}_x]_{0.1}$ to 1.7 in $[\text{NH}_x]_{0.4}$ (Fig. S65). The increase in pH incentivize the uptake and dissociation of semi-volatile and moderately acidic species such as MSIA, which aids the production of MSA in the aqueous-phase. The $\text{MSA}/\text{SO}_4^{2-}$ PM ratio consequently increases from 2.1 in $[\text{NH}_x]_{0.1}$ to 2.5 in $[\text{NH}_x]_{0.4}$.

The biggest impact from changes in the NH_x concentration nevertheless concerns the rate of SA- NH_3 driven nucleation. On the third day of the simulation, the gas-phase NH_3 concentration in $[\text{NH}_x]_{0.4}$ is 7.3 times higher than in $[\text{NH}_x]_{0.1}$, which in turn increases the SA- NH_3 nucleation rate by a factor of 22.9. As a result, the nucleation rate in $[\text{NH}_x]_{0.1}$ is insufficient to initiate a distinct growth event and, consequently, to form and sustain an Aitken mode throughout the simulation (Fig. S64). At a concentration of 0.2 mmol/m^3 , however, the NH_3 gas-phase concentration becomes sufficiently high to allow the particles to form and grow into the Aitken mode. Increasing the NH_x concentration further mainly impacts the nucleation rate and thus the PN concentration in the DMS-derived growth mode. Consequently, the total PN concentration increases from $4.1 \times 10^2 \text{ cm}^{-3}$ in $[\text{NH}_x]_{0.2}$ to $1.1 \times 10^3 \text{ cm}^{-3}$ in $[\text{NH}_x]_{0.3}$ and $1.5 \times 10^3 \text{ cm}^{-3}$ in $[\text{NH}_x]_{0.4}$ (Fig. 3k). The mode diameter at the end of the simulation is impacted by the rate of nucleation. As a result, more SA is needed to grow the particles in $[\text{NH}_x]_{0.4}$ which stunts their growth compared to the particles in $[\text{NH}_x]_{0.2}$. The newly formed particles therefore reach a mode diameter at the end of the simulation of 90 nm (25th-75th prct.: 76-107 nm) in $[\text{NH}_x]_{0.2}$ and 67 nm (25th-75th prct.: 56-81 nm) in $[\text{NH}_x]_{0.4}$ (Fig. 3l).

615 3.2.7 Clouds

In the BaseCase model setup, the first two days of the simulation includes partial cloud cover during midday and midnight. The following four days contain no clouds. In the CLOUD sensitivity run, clouds are introduced at midday and midnight throughout the simulation. As a consequence, the total source flux of CH_3SO_2 , CH_3SO_3 and SA decreases as the water soluble compounds DMSO, MSIA and SO_2 are lost to the aqueous-phase during cloud cover (Fig. S81 and S82). The gas-phase concentration of SO_2 is affected in particular by the presence of clouds, as it does not partition readily to the deliquesced

620



particles. Therefore, SO_2 becomes insignificant in the production of SA during cloudy conditions compared to the decomposition of CH_3SO_3 which makes up 97% of the SA source flux throughout the CLOUD sensitivity run as opposed to 89 % in BaseCase. The combination of the uptake of MSIA and SO_2 during the additional cloud-periods lowers the total SA source flux from $4.1 \times 10^3 \text{ cm}^{-3}\text{s}^{-1}$ in BaseCase to $1.9 \times 10^3 \text{ cm}^{-3}\text{s}^{-1}$ in CLOUD.

625

The total DMS-derived production of secondary aerosol PM nevertheless increases by 71% as the SO_2 taken up during the cloud periods is transformed efficiently to SO_4^{2-} PM. The impact is evident from the $\text{MSA}/\text{SO}_4^{2-}$ PM ratio which drops from 2.5 to 0.7, almost exclusively driven by the increase in SO_4^{2-} PM as MSA is produced efficiently in the absence of clouds through the uptake and aqueous-phase processing of MSIA in the deliquesced aerosol particles. On day three of the simulation, the NPF event initiates in similar fashion to the event in the BaseCase simulation, but loses momentum after the first midday cloud period (Fig. S74). This happens as the uptake of DMSO, MSIA, SO_2 and SA to the aqueous-phase in addition to the aqueous-phase processing of DMSO, MSIA and SO_2 ensures that the gas-phase concentration of these species must rebuild after each midday cloud period (Fig. S73). The same goes for NH_3 , which is not able to reach sufficient concentrations in the gas-phase in order to drive additional NPF or neutralize the newly formed particles. As a consequence, additional NPF after the cloud-event on day three of the simulation becomes negligible as the SA-concentration in the gas-phase is not sufficient to sustain the growth into the nucleation mode. Therefore, no distinct growth mode forms after the precipitation event in the CLOUD sensitivity run. The overall effect of clouds are therefore to terminate both the formation of DMS-derived particles and their growth into the nucleation and Aitken mode size range.

630

635

3.3 Impact of chemistry

Although this study has demonstrated that DMS is able to drive the formation and growth of aerosol particles within the pristine MBL under various metrological and hydrological conditions, some uncertainty still remains due to present representation of the DMS oxidation mechanism. Most of this uncertainty lies in the fate of MSIA and its successors CH_3SO_2 and CH_3SO_3 , due to their role in the production of SA and MSA. CH_3SO_2 and CH_3SO_3 are also formed in the DMS abstraction pathway, but since HPMTF and SO_2 make up the major products from said pathway the production of CH_3SO_2 and CH_3SO_3 remains small. At 283K, MSIA oxidation by OH makes up 96% of the CH_3SO_2 source flux while the isomerization of CH_3SOO makes up 4%. At the low NO_x conditions representative of the pristine MBL, CH_3SO_2 formation through the reaction of CH_3SO with NO_2 or CH_3SOO_2 with NO becomes insignificant. The role of MSIA in the production of SA through CH_3SO_2 and CH_3SO_3 is evident from the 'noMSIAabs' sensitivity run. Here, the source flux of SA decreases by 87% throughout the simulation, thus decreasing the strength of the NPF event following the precipitation event on day three (Figure 4a and S10.2). This is caused by SA being formed predominantly through SO_2 which is slower than the production of SA through the thermal decomposition of CH_3SO_3 . Consequently, SA is not formed fast enough to initiate a strong NPF and growth event before the concentration of sea spray becomes to high. Some new particles are able to form on days 4-6 of the simulation when the SO_2 concentration has had time to accumulate, but the nucleation and growth rate remains limited. The rate of the H-abstraction from MSIA by OH was originally determined experimentally at 298K by Kukui et al. (2003). In this work, we extend the rate

650

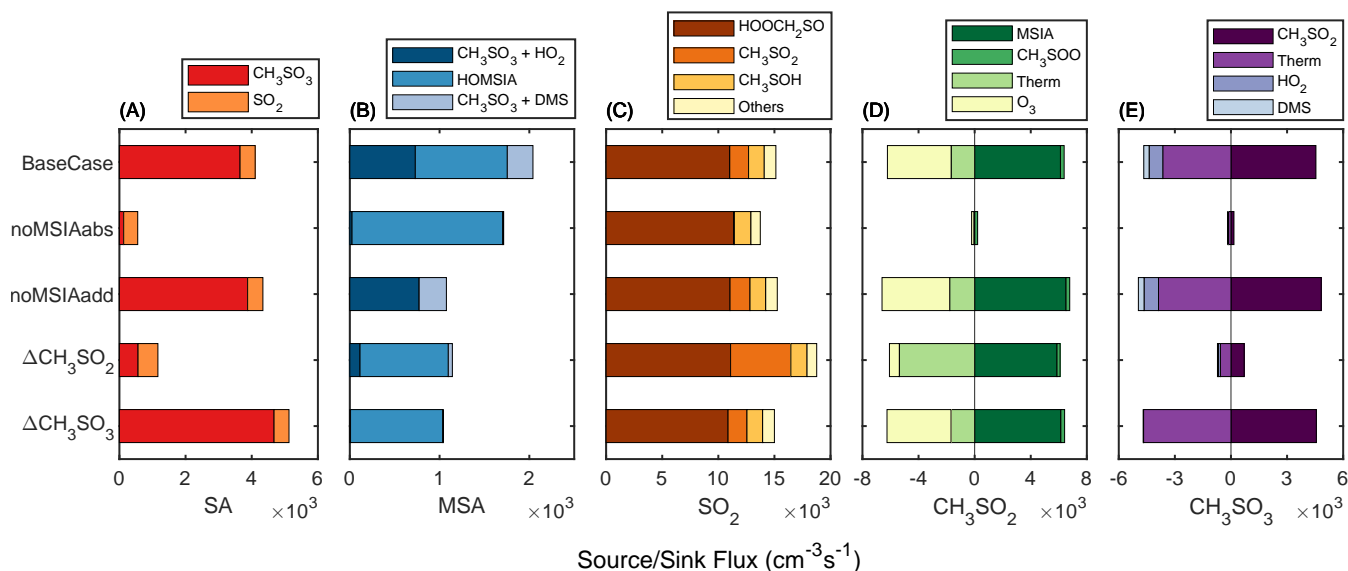


Figure 4. Gas-phase sink and/or source fluxes for SA, MSA, SO_2 , CH_3SO_2 , and CH_3SO_3 . The legend for the source flux refers to the precursor of the compound in question, while for the sink flux it refers to the oxidant or process that reacts with or transforms the compound. 'Therm' denotes the thermal decomposition of either CH_3SO_2 or CH_3SO_3 .

655 determined by Kukui et al. (2003) with a theoretical temperature dependency based on quantum chemical calculations. Said temperature dependency predicts a slight increase in the rate of H-abstraction at lower temperatures, e.g. $9.0 \times 10^{-11} \text{ cm}^3 \text{ s}^{-1}$ at 298K and $1.2 \times 10^{-10} \text{ cm}^3 \text{ s}^{-1}$ at 273K. It should be noted that in the simulation the increase in the H-abstraction rate is counterbalanced by the decrease in the OH concentration at lower temperatures.

660 In addition to adding temperature dependency to the rate for H-abstraction from MSIA by OH, this study also presents the temperature dependant reaction rate for the addition of OH to MSIA and subsequent production of MSA through H-abstraction by O_2 . This pathway has been discussed in previous publications (Lucas and Prinn, 2002; Shen et al., 2022; Ye et al., 2022), but so far no experimental nor theoretical reaction rates have been determined. Here, quantum chemical calculations are used to provide the reaction rate. The noMSIAadd sensitivity run demonstrates the impact of the reaction, which has little influence
 665 on the formation and initial growth of the aerosol particles as it does not significantly influence the production of SA. It does however impact the gas-phase production of MSA which decreases by 47% throughout the simulation (Fig. 4b). As a result, including this reaction pathway might help to improve model representations of MSA in the gas-phase. The HO-MSIA intermediate that forms after the OH-addition to MSIA has also been shown to form H_2SO_3 (and thus eventually SO_2) in other studies by the loss of a methyl group (Lv et al., 2019; Berndt et al., 2024). In accordance with the calculations performed in
 670 this study, however, the H-abstraction by O_2 forming MSA is considerably faster than the decomposition to H_2SO_3 (2.4×10^{13}



s^{-1} and $6.4 \times 10^{10} \text{ s}^{-1}$ at 283K and 1 atm, respectively).

Another aspect of the DMS oxidation mechanism that adds uncertainty to the role of DMS in NPF in the MBL is the rate for the thermal decomposition of CH_3SO_2 and CH_3SO_3 into SO_2 and SO_3 , respectively. Unfortunately, it is challenging
675 to calculate the transition state for the decomposition of both these species and therefore a theoretical rate has not been determined in this study. Instead we demonstrate the impact that these rates have on DMS-derived NPF in the MBL through sensitivity runs performed with the experimentally determined or estimated rates that are currently available in the literature. In this study we use the rates prescribed by MCMv3.3.1 in the BaseCase setup as they are in line with the experimental rate for the CH_3SO_2 decomposition obtained by Borissenko et al. (2003) (e.g. $< 1 \text{ s}^{-1}$ at 298K). Higher rates for the decompo-
680 sition of CH_3SO_2 have been estimated in the studies by Jacob et al. (2024) (8.3 s^{-1} at 298K) and Berndt et al. (2023) (20 s^{-1}). As for the decomposition of CH_3SO_3 , Cao et al. (2013) calculated an upper limit of 12.7 s^{-1} at 298K while an estimate based on experimental results by Berndt et al. (2023) falls in line with the rate presented in MCMv3.3.1 (0.1 s^{-1} at 298K).

In the $\Delta\text{CH}_3\text{SO}_2$ sensitivity run, the rate for the thermal decomposition of CH_3SO_2 was increased in accordance with the
685 rate estimated by Jacob et al. (2024). This increase favours the production of SO_2 , the source flux of which increases by 24% throughout the simulation at the expense of CH_3SO_3 and thus SA, the source flux of which decreases by 72% (Fig. 4c and 4a). The decrease in SA lowers the nucleation rate on day three from $0.13 \text{ cm}^{-3}\text{s}^{-1}$ to $8.7 \times 10^{-2} \text{ cm}^{-3}\text{s}^{-1}$ and causes the particles to reach a mode diameter of 52 nm (25th-75th prct.: 41-65 nm) at the end of the simulation compared to 73 nm (25th-75th prct.: 60-88 nm) in BaseCase. Due to the decrease in the CH_3SO_3 concentration, SO_2 becomes more important for
690 the production of SA making up 52% of the SA source flux as opposed to 11% in the BaseCase simulation. The conversion of SO_2 to SO_3 and thus SA nevertheless remains slow, meaning that new particles are not able to form efficiently before the concentration of sea spray particles and thus the SA condensation sink becomes to high (Fig. S84). Using the rate by Jacob et al. (2024) also impacts the source flux of MSA in the gas-phase which decreases by 44% as a result of the decrease in the CH_3SO_3 concentration. As a consequence, MSA production through OH addition to MSIA becomes the dominating source
695 of MSA in the gas-phase comprising 86% of the MSA gas-phase source flux compared to 50% in the BaseCase simulation. In summery, a higher rate for the thermal decomposition of CH_3SO_2 would make DMS-driven NPF in the MBL less favourable as the direct production of SA is suppressed.

A higher rate for the thermal decomposition of CH_3SO_3 , however, is seen to have the opposite effect. Increasing said rate
700 favours the production of SO_3 and SA as opposed to MSA. This is evident from the $\Delta\text{CH}_3\text{SO}_3$ sensitivity run where the rate for the thermal decomposition of $\Delta\text{CH}_3\text{SO}_3$ was increased in accordance with the study by Cao et al. (2013). As a consequence, the total SA source flux showed a 25% increase compared to the BaseCase run at the expense of the MSA source flux in the gas-phase which decreases by 49%. Said decrease originates from the reaction of CH_3SO_3 with HO_2 and DMS, respectively, which make up $\sim 1\%$ of the MSA source in the $\Delta\text{CH}_3\text{SO}_3$ sensitivity run. Consequently, MSA production through OH
705 addition to MSIA as proposed in this study becomes the almost exclusive source of MSA in the gas phase. The impact of the



increase in the SA source flux from the increase in the thermal decomposition of CH_3SO_3 is evident from the the SA- NH_3 derived nucleation rate. On day three of the simulation, the nucleation rate increases by 19%, ultimately increasing the total PN concentration at the end of the simulation from $1.1 \times 10^3 \text{ cm}^{-3}$ in BaseCase to $1.2 \times 10^3 \text{ cm}^{-3}$ in $\Delta\text{CH}_3\text{SO}_3$. The increase in the PN concentration counterbalances the increase in the growth for the individual aerosol particles as more SA is needed to grow the newly formed particles into the nucleation and Aitken mode size range. As a result, the mode diameter of the growth mode at the end of simulation is lower at 68 nm (25th-75th prct.: 57-82 nm) in $\Delta\text{CH}_3\text{SO}_3$ compared to 73 nm (25th-75th prct.: 60-88 nm) in BaseCase, despite the increase in the SA source flux.

The rate calculated by Cao et al. (2013) nevertheless remains uncertain. In the review article by Barnes et al. (2006), it is mentioned that the rate for the thermal decomposition of CH_3SO_3 should be similar or much lower than the one by CH_3SO_2 . This is supported by a recent experimental study by Berndt et al. (2023), where they estimate said rate to be similar to the one presented in the MCMv3.3.1. It remains evident however that the rate for the thermal decomposition of both CH_3SO_2 and CH_3SO_3 has an impact on the formation and growth of DMS-derived aerosol particles in the MBL. At the moment, any claim that these rates should be higher than those presented in the MCMv3.3.1 are based on estimates and theoretical calculations. It remains essential therefore that the thermal decomposition of both CH_3SO_2 and CH_3SO_3 are examined further in laboratory studies so as to decrease the uncertainty linked to their role in the formation and growth of aerosol particles from DMS.

4 Conclusions

Advanced simulations of atmospheric chemistry and aerosol dynamics in a pristine ocean scenario shows that natural emissions of DMS and NH_3 are able to drive SA- NH_3 -derived NPF within the MBL, the particles of which are able to grow into the upper Aitken and accumulation mode size range with the potential to act as CCN. The formation and growth of said particles is favoured during cloud-free conditions following an event of moderate to heavy precipitation. Precipitation effectively lowers the concentrations of sea spray aerosol PM in the MBL, allowing SA to reach concentrations where they are able to cluster with NH_3 and grow into the nucleation and Aitken mode size range.

The formation and growth of the particles are impacted by various metrological and hydrological conditions. Low temperatures favour SA- NH_3 NPF by preventing cluster evaporation, but at the same impair NPF and growth as they promote the uptake of MSIA to the sea spray particles which lowers the production of SA. High temperatures, on the other hand, prevent NPF and growth by favouring the DMS abstraction pathway over the addition pathway. Moreover, the thermal decomposition of CH_3SO_2 into CH_3OO and SO_2 reduces the production of CH_3SO_3 , thereby lowering the formation of SA. This leads to optimal DMS-derived particle growth at moderate temperatures (283-288 K). Varying wind-speed conditions produce similar results: low wind speeds limit NPF and growth due to reduced emissions of DMS and NH_3 , whereas high wind speeds constrain particle growth by increasing the sea spray PM, which enhances the uptake of MSIA and SA to the particle phase. Consequently, DMS-derived particles in the MBL grow most efficiently at moderate wind-speeds around 4-6 m/s. Sensitivity



740 runs utilizing different rates of precipitation demonstrates that DMS and NH_3 are able to drive NPF and growth in the MBL,
even during conditions with a moderate rainfall (2.5-5.0 mm/h). At 10 mm/h and beyond, the far majority (> 98%) of sea
spray aerosol PM has been removed, providing optimal conditions for NPF and growth. Increasing the SST promotes the
ocean-air flux of DMS and NH_3 , which in turn favours the formation and growth of DMS-derived aerosol particles despite the
increase in sea-spray PM. For the surface ocean concentrations of DMS, the SA production and subsequent aerosol particle
745 OH. The acidification of the particles with higher emissions of DMS also limits the NH_3 concentrations in the gas-phase, ulti-
mately lowering the rate of nucleation. For the sea surface concentration of NH_x , 0.2 mmol/m^3 was sufficient to initiate and
sustain a DMS-derived growth event, with higher concentrations promoting the rate of SA- NH_3 nucleation and neutralization
of the aerosol particles. If sporadic cloud cover is introduced in the model following the precipitation event, NPF is terminated
and the particles are not able to form a distinct growth event.

750

The degree to which DMS is able to form and sustain the growth of new particles within the MBL also depends heavily
on the representation of the DMS oxidation mechanism. MSIA is found to be one of the key components in this process, as it
governs the direct production of SA through the formation of CH_3SO_2 and CH_3SO_3 . Omitting the H-abstraction from MSIA
by OH from the model decreases the SA production to a point where NPF is heavily limited and the particles that do form are
755 unlikely to reach the Aitken mode. Omitting the addition of OH to MSIA (as presented in this study) does not impact NPF
significantly. It does, however, decrease the production of MSA in the gas-phase substantially. The spread in the rate for the
thermal decomposition of CH_3SO_2 and CH_3SO_3 as presented in the literature proves to be a big source of uncertainty in the
direct production of SA and thus DMS-derived NPF and growth. High estimates for $k_{\Delta\text{CH}_3\text{SO}_2}$ promotes SO_2 production at
the expense of CH_3SO_3 , slowing down the formation SA and thus limiting NPF and growth. High estimates for $k_{\Delta\text{CH}_3\text{SO}_3}$,
760 on the other hand, promotes direct SA production and thus NPF. Future work, therefore, should focus on improving the rate
coefficients for these reactions.

As the observations on NPF over the oceans remains scarce, we also urge the scientific community to provide more and
better measurements from the marine environment. Given that the current observations on NPF in the MBL is based mainly on
765 flight and ship campaigns (Baccarini et al., 2021; Zheng et al., 2021), long term measurements in pristine ocean conditions are
needed to better quantify the impact of NPF on CCN concentrations in the MBL.

Author contributions. R.W.d.J. designed and planned the study, performed the ADCHAM simulations, interpreted and visualized the results,
and wrote the paper. P.R. and R.W.d.J. developed the ADCHAM model. Z.F. performed the quantum chemical calculations. M.B. supervised
the project.



770 *Competing interests.* The authors declare that they have no conflict of interest.

Acknowledgements. R.W.d.J would like to thank the Carlsberg Foundation (project no. CF24-1915) for funding this research. Partially, funding was also provided by the AoF project ACCC, “The Atmosphere and Climate Competence Center,” under grant agreement no. 337549. The model work was supported by the Swedish strategic research area: Modelling the Regional and Global Earth system (MERGE) and the Lund University Faculty of Engineering Profile Area: AEROSOLS. Z.F. thanks the National Natural Science Foundation of China
775 (project no. 22306002).



References

- BIOVIA COSMOtherm, Release 2021; Dassault Systèmes. <http://www.3ds.com>, 2021.
- Adler, T., Knizia, G., and Werner, H.-J.: A simple and efficient CCSD(T)-F12 approximation, *The Journal of chemical physics*, 127, 221 106, <https://doi.org/10.1063/1.2817618>, 2008.
- 780 Baccarini, A., Dommen, J., Lehtipalo, K., Henning, S., Modini, R., Gysel, M., Baltensperger, U., and Schmale, J.: Low-Volatility Vapors and New Particle Formation Over the Southern Ocean During the Antarctic Circumnavigation Expedition, *Journal of Geophysical Research: Atmospheres*, 126, <https://doi.org/10.1029/2021JD035126>, 2021.
- Barnes, I., Hjorth, J., and Mihalopoulos, N.: Dimethyl Sulfide and Dimethyl Sulfoxide and Their Oxidation in the Atmosphere, *Chemical Reviews*, 106, 940–975, <https://doi.org/10.1021/cr020529+>, 2006.
- 785 Barthel, S., Tegen, I., and Wolke, R.: Do new sea spray aerosol source functions improve the results of a regional aerosol model?, *Atmospheric Environment*, 198, 265–278, <https://doi.org/https://doi.org/10.1016/j.atmosenv.2018.10.016>, 2019.
- Bates, T., Lamb, B., Guenther, A., Dignon, J., and Stoiber, R.: Sulfur Emissions to the Atmosphere from Natural Sources, *Journal of Atmospheric Chemistry*, 14, 315–337, <https://doi.org/10.1007/BF00115242>, 1992.
- Beck, L., Sarnela, N., Junninen, H., Hoppe, C., Garmash, O., Bianchi, F., Riva, M., Rose, C., Peräkylä, O., Wimmer, D., Kausiala, O.,
790 Jokinen, T., Ahonen, L., Mikkilä, J., Hakala, J., He, X.-C., Kontkanen, J., Wolf, K., Cappelletti, D., and Sipilä, M.: Differing Mechanisms of New Particle Formation at Two Arctic Sites, *Geophysical Research Letters*, 48, <https://doi.org/10.1029/2020GL091334>, 2021.
- Berndt, T., Scholz, W., Mentler, B., Fischer, L., Hoffmann, E., Tilgner, A., Hyttinen, N., Prisle, N. L., Hansel, A., and Herrmann, H.: Fast Peroxy Radical Isomerization and OH Recycling in the Reaction of OH Radicals with Dimethyl Sulfide, *The Journal of Physical Chemistry Letters*, 2019, <https://doi.org/10.1021/acs.jpcclett.9b02567>, 2019.
- 795 Berndt, T., Hoffmann, E., Tilgner, A., Stratmann, F., and Herrmann, H.: Direct sulfuric acid formation from the gas-phase oxidation of reduced-sulfur compounds, *Nature Communications*, 14, <https://doi.org/10.1038/s41467-023-40586-2>, 2023.
- Berndt, T., Hoffmann, E. H., Tilgner, A., and Herrmann, H.: Gas-Phase Formation of Sulfurous Acid (H₂SO₃) in the Atmosphere, *Angewandte Chemie International Edition*, 63, e202405 572, <https://doi.org/https://doi.org/10.1002/anie.202405572>, 2024.
- Besel, V., Kubecka, J., Kurtén, T., and Vehkamäki, H.: Impact of Quantum Chemistry Parameter Choices and Cluster Distribution Model Settings on Modeled Atmospheric Particle Formation Rates, *The Journal of Physical Chemistry A*, XXXX,
800 <https://doi.org/10.1021/acs.jpca.0c03984>, 2020.
- Blomquist, B. W., Brumer, S. E., Fairall, C. W., Huebert, B. J., Zappa, C. J., Brooks, I. M., Yang, M., Bariteau, L., Prytherch, J., Hare, J. E., Czerski, H., Matei, A., and Pascal, R. W.: Wind Speed and Sea State Dependencies of Air-Sea Gas Transfer: Results From the High Wind Speed Gas Exchange Study (HiWinGS), *Journal of Geophysical Research: Oceans*, 122, 8034–8062,
805 <https://doi.org/https://doi.org/10.1002/2017JC013181>, 2017.
- Borissenko, D., Kukui, A., Laverdet, G., and Le Bras, G.: Experimental Study of SO₂ Formation in the Reactions of CH₃SO Radical with NO₂ and O₃ in Relation with the Atmospheric Oxidation Mechanism of Dimethyl Sulfide, *The Journal of Physical Chemistry A*, 107, 1155–1161, <https://doi.org/10.1021/jp021701g>, 2003.
- Brauer, P., Tilgner, A., Wolke, R., and Herrmann, H.: Mechanism development and modelling of tropospheric multiphase halogen chemistry: The CAPRAM Halogen Module 2.0 (HM2), *JOURNAL OF ATMOSPHERIC CHEMISTRY*, 70, 19–52, <https://doi.org/10.1007/s10874-013-9249-6>, 2013.



- Brean, J., Dall'osto, M., Simó, R., Shi, Z., Beddows, D., and Harrison, R.: Open ocean and coastal new particle formation from sulfuric acid and amines around the Antarctic Peninsula, *Nature Geoscience*, 14, <https://doi.org/10.1038/s41561-021-00751-y>, 2021.
- Canneaux, S., Bohr, F., and Henon, E.: KiSThelP: a program to predict thermodynamic properties and rate constants from quantum chemistry results, *Journal of Computational Chemistry*, 35, 82–93, 2014.
- 815 Cao, J., WANG, W.-L., GAO, L.-J., and FU, F.: Mechanism and Thermodynamic Properties of CH₃SO₃ Decomposition, *Acta Physico-Chimica Sinica*, 29, <https://doi.org/10.3866/PKU.WHXB201304021>, 2013.
- Charlson, R. J., Lovelock, J. E., Andreae, M. O., and Warren, S. G.: Oceanic phytoplankton, atmospheric sulphur, cloud albedo and climate, *Nature*, 326, 655–661, <https://doi.org/10.1038/326655a0>, 1987.
- 820 Dall'osto, M., Geels, C., Beddows, D. C. S., Boertmann, D., Lange, R., Nøjgaard, J. K., Harrison, R. M., Simo, R., Skov, H., and Massling, A.: Regions of open water and melting sea ice drive new particle formation in North East Greenland, *Scientific Reports*, 8, 6109, <https://doi.org/10.1038/s41598-018-24426-8>, 2018.
- D'Ambro, E., Hyttinen, N., Møller, K., Iyer, S., Otkjær, R., Bell, D., Liu, J., Lopez-Hilfiker, F., Schobesberger, S., Shilling, J., Zelenyuk, A., Kjaergaard, H., Thornton, J., and Kurtén, T.: Pathways to Highly Oxidized Products in the Δ^3 -Carene + OH System, *Environmental Science & Technology*, 56, <https://doi.org/10.1021/acs.est.1c06949>, 2022.
- 825 Eckart, C.: The penetration of a potential barrier by electrons, *Physical Review*, 35, 1303–1309, 1930.
- Elm, J., Kubečka, J., Besel, V., Jääskeläinen, M. J., Halonen, R., Kurtén, T., and Vehkamäki, H.: Modeling the formation and growth of atmospheric molecular clusters: A review, *Journal of Aerosol Science*, 149, 105621, <https://doi.org/https://doi.org/10.1016/j.jaerosci.2020.105621>, 2020.
- 830 Frisch, M. J., Trucks, G. W., Schlegel, H. B., Scuseria, G. E., Robb, M. A., Cheeseman, J. R., Scalmani, G., Barone, V., Petersson, G. A., Nakatsuji, H., Li, X., Caricato, M., Marenich, A. V., Bloino, J., Janesko, B. G., Gomperts, R., Mennucci, B., Hratchian, H. P., Ortiz, J. V., Izmaylov, A. F., Sonnenberg, J. L., Williams-Young, D., Ding, F., Lipparini, F., Egidi, F., Goings, J., Peng, B., Petrone, A., Henderson, T., Ranasinghe, D., Zakrzewski, V. G., Gao, J., Rega, N., Zheng, G., Liang, W., Hada, M., Ehara, M., Toyota, K., Fukuda, R., Hasegawa, J., Ishida, M., Nakajima, T., Honda, Y., Kitao, O., Nakai, H., Vreven, T., Throssell, K., Montgomery, J. A. J., Peralta, J. E., Ogliaro, F.,
- 835 Bearpark, M. J., Heyd, J. J., Brothers, E. N., Kudin, K. N., Staroverov, V. N., Keith, T. A., Kobayashi, R., Normand, J., Raghavachari, K., Rendell, A. P., Burant, J. C., Iyengar, S. S., Tomasi, J., Cossi, M., Millam, J. M., Klene, M., Adamo, C., Cammi, R., Ochterski, J. W., Martin, R. L., Morokuma, K., Farkas, O., Foresman, J. B., and Fox, D. J.: *Gaussian 16*, Revision B.01, 2016.
- Fu, Z., Xie, H. B., Elm, J., Liu, Y., Fu, Z., and Chen, J.: Atmospheric autoxidation of organophosphate esters, *Environmental Science & Technology*, 56, 6944–6955, 2022.
- 840 Fu, Z., Guo, S., Xie, H.-B., Zhou, P., Boy, M., Yao, M., and Hu, M.: A Near-Explicit Reaction Mechanism of Chlorine-Initiated Limonene: Implications for Health Risks Associated with the Concurrent Use of Cleaning Agents and Disinfectants, *Environmental Science & Technology*, 58, 19762–19773, 2024a.
- Fu, Z., Guo, S., Yu, Y., Xie, H.-B., Li, S., Lv, D., Zhou, P., Song, K., Chen, Z., Tan, R., Hu, K., Shen, R., Yao, M., and Hu, M.: Oxidation Mechanism and Toxicity Evolution of Linalool, a Typical Indoor Volatile Chemical Product, *Environmental Health*, 2, 486–498, 2024b.
- 845 Hoffmann, E. H., Tilgner, A., Schrödner, R., Bräuer, P., Wolke, R., and Herrmann, H.: An advanced modeling study on the impacts and atmospheric implications of multiphase dimethyl sulfide chemistry, *Proceedings of the National Academy of Sciences*, 113, 11776–11781, <https://doi.org/10.1073/pnas.1606320113>, 2016.



- Hulswar, S., Simó, R., Galí, M., Bell, T. G., Lana, A., Inamdar, S., Halloran, P. R., Manville, G., and Mahajan, A. S.: Third revision of the global surface seawater dimethyl sulfide climatology (DMS-Rev3), *Earth System Science Data*, 14, 2963–2987, <https://doi.org/10.5194/essd-14-2963-2022>, 2022.
- Jacob, L. S. D., Giorio, C., and Archibald, A. T.: Extension, development, and evaluation of the representation of the OH-initiated dimethyl sulfide (DMS) oxidation mechanism in the Master Chemical Mechanism (MCM) v3.3.1 framework, *Atmospheric Chemistry and Physics*, 24, 3329–3347, <https://doi.org/10.5194/acp-24-3329-2024>, 2024.
- Jacobson, M. Z.: *Fundamentals of Atmospheric Modeling*, Cambridge University Press, 2 edn., <https://doi.org/10.1017/CBO9781139165389>, 2005.
- Jenkin, M. E., Saunders, S. M., and Pilling, M. J.: The tropospheric degradation of volatile organic compounds: a protocol for mechanism development, *Atmospheric Environment*, 31, 81 – 104, [https://doi.org/https://doi.org/10.1016/S1352-2310\(96\)00105-7](https://doi.org/https://doi.org/10.1016/S1352-2310(96)00105-7), 1997.
- Jenkin, M. E., Saunders, S. M., Wagner, V., and Pilling, M. J.: Protocol for the development of the Master Chemical Mechanism, MCM v3 (Part B): tropospheric degradation of aromatic volatile organic compounds, *Atmospheric Chemistry and Physics*, 3, 181–193, <https://doi.org/10.5194/acp-3-181-2003>, 2003.
- Johnson, M. T., Liss, P. S., Bell, T. G., Lesworth, T. J., Baker, A. R., Hind, A. J., Jickells, T. D., Biswas, K. F., Woodward, E. M. S., and Gibb, S. W.: Field observations of the ocean-atmosphere exchange of ammonia: Fundamental importance of temperature as revealed by a comparison of high and low latitudes, *Global Biogeochemical Cycles*, 22, <https://doi.org/https://doi.org/10.1029/2007GB003039>, 2008.
- Jokinen, T., Sipilä, M., Kontkanen, J., Vakkari, V., Tisler, P., Duplissy (née Kyrö), E.-M., Junninen, H., Kangasluoma, J., Manninen, H., Petäjä, T., Kulmala, M., Worsnop, D., Kirkby, J., Virkkula, A., and Kerminen, V.-M.: Ion-induced sulfuric acid–ammonia nucleation drives particle formation in coastal Antarctica, *Science Advances*, 4, eaat9744, <https://doi.org/10.1126/sciadv.aat9744>, 2018.
- Kirkby, J., Curtius, J., Almeida, J., Dunne, E., Duplissy, J., Ehrhart, S., Franchin, A., Gagné, S., Ickes, L., Kürten, A., Kupc, A., Metzger, A., Riccobono, F., Rondo, L., Schobesberger, S., Tsagkogeorgas, G., Wimmer, D., Amorim, A., Bianchi, F., and Kulmala, M.: Role of sulphuric acid, ammonia and galactic cosmic rays in atmospheric aerosol nucleation, *Nature*, 476, 429–33, <https://doi.org/10.1038/nature10343>, 2011.
- Korhonen, P., Kulmala, M., Laaksonen, A., Viisanen, Y., McGraw, R., and Seinfeld, J. H.: Ternary nucleation of H₂SO₄, NH₃, and H₂O in the atmosphere, *Journal of Geophysical Research: Atmospheres*, 104, 26 349–26 353, <https://doi.org/10.1029/1999JD900784>, 1999.
- Kukui, A., Borissenko, D., Laverdet, G., and Bras, G.: Gas-Phase Reactions of OH Radicals with Dimethyl Sulfoxide and Methane Sulfinic Acid Using Turbulent Flow Reactor and Chemical Ionization Mass Spectrometry, *Journal of Physical Chemistry A*, 107, <https://doi.org/10.1021/jp0276911>, 2003.
- Kulmala, M., Kontkanen, J., Junninen, H., Lehtipalo, K., Manninen, H. E., Nieminen, T., Petäjä, T., Sipilä, M., Schobesberger, S., Rantala, P., Franchin, A., Jokinen, T., Järvinen, E., Äijälä, M., Kangasluoma, J., Hakala, J., Aalto, P. P., Paasonen, P., Mikkilä, J., Vanhanen, J., Aalto, J., Hakola, H., Makkonen, U., Ruuskanen, T., Mauldin, R. L., Duplissy, J., Vehkamäki, H., Bäck, J., Kortelainen, A., Riipinen, I., Kurtén, T., Johnston, M. V., Smith, J. N., Ehn, M., Mentel, T. F., Lehtinen, K. E. J., Laaksonen, A., Kerminen, V.-M., and Worsnop, D. R.: Direct Observations of Atmospheric Aerosol Nucleation, *Science*, 339, 943–946, <https://doi.org/10.1126/science.1227385>, 2013.
- Laakso, L., Grönholm, T., Üllar Rannik, Kosmale, M., Fiedler, V., Vehkamäki, H., and Kulmala, M.: Ultrafine particle scavenging coefficients calculated from 6 years field measurements, *Atmospheric Environment*, 37, 3605–3613, [https://doi.org/https://doi.org/10.1016/S1352-2310\(03\)00326-1](https://doi.org/https://doi.org/10.1016/S1352-2310(03)00326-1), 2003.



- Lana, A., Bell, T. G., Simó, R., Vallina, S. M., Ballabrera-Poy, J., Kettle, A. J., Dachs, J., Bopp, L., Saltzman, E. S., Stefels, J., Johnson, J. E., and Liss, P. S.: An updated climatology of surface dimethylsulfide concentrations and emission fluxes in the global ocean, *Global Biogeochemical Cycles*, 25, <https://doi.org/10.1029/2010GB003850>, 2011.
- Liss, P. S. and Merlivat, L.: *Air-Sea Gas Exchange Rates: Introduction and Synthesis*, pp. 113–127, Springer Netherlands, Dordrecht, ISBN 978-94-009-4738-2, https://doi.org/10.1007/978-94-009-4738-2_5, 1986.
- Lovelock, J. E., Maggs, R. J., and Rasmussen, R. A.: Atmospheric Dimethyl Sulfide and the Natural Sulfur Cycle, *Nature*, 237, 452–453, 1972.
- Lucas, D. D. and Prinn, R. G.: Mechanistic studies of dimethylsulfide oxidation products using an observationally constrained model, *Journal of Geophysical Research: Atmospheres*, 107, ACH 12–1–ACH 12–26, <https://doi.org/10.1029/2001JD000843>, 2002.
- Lv, G., Zhang, C., and Sun, X.: Understanding the oxidation mechanism of methanesulfinic acid by ozone in the atmosphere, *Scientific Reports*, 9, 322, <https://doi.org/10.1038/s41598-018-36405-0>, 2019.
- McGrath, M. J., Olenius, T., Ortega, I. K., Loukonen, V., Paasonen, P., Kurtén, T., Kulmala, M., and Vehkamäki, H.: Atmospheric Cluster Dynamics Code: A Flexible Method for Solution of the Birth-Death Equations, *Atmos. Chem. Phys.*, 12, 2345–2355, 2012.
- Merikanto, J., Spracklen, D., Mann, G., Pickering, S., and Carslaw, K.: Impact of nucleation on global CCN, *Atmospheric Chemistry and Physics*, 9, <https://doi.org/10.5194/acp-9-8601-2009>, 2009.
- Møller, K. H., Bates, K. H., and Kjaergaard, H. G.: The Importance of Peroxy Radical Hydrogen-Shift Reactions in Atmospheric Isoprene Oxidation, 123, 920–932, <https://doi.org/10.1021/acs.jpca.8b10432>, epub 2019-01-23, 2019.
- Nightingale, P. D., Malin, G., Law, C. S., Watson, A. J., Liss, P. S., Liddicoat, M. I., Boutin, J., and Upstill-Goddard, R. C.: In situ evaluation of air-sea gas exchange parameterizations using novel conservative and volatile tracers, *Global Biogeochemical Cycles*, 14, 373–387, <https://doi.org/10.1029/1999GB900091>, 2000.
- Olenius, T., Kupiainen-Määttä, O., Ortega, I., Kurtén, T., and Vehkamäki, H.: Free energy barrier in the growth of sulfuric acid-ammonia and sulfuric acid-dimethylamine clusters, *The Journal of chemical physics*, 139, 084 312, <https://doi.org/10.1063/1.4819024>, 2013.
- Paulot, F., Jacob, D. J., Johnson, M. T., Bell, T. G., Baker, A. R., Keene, W. C., Lima, I. D., Doney, S. C., and Stock, C. A.: Global oceanic emission of ammonia: Constraints from seawater and atmospheric observations, *Global Biogeochemical Cycles*, 29, 1165–1178, <https://doi.org/10.1002/2015GB005106>, 2015.
- Paulot, F., Stock, C., John, J. G., Zadeh, N., and Horowitz, L. W.: Ocean Ammonia Outgassing: Modulation by CO₂ and Anthropogenic Nitrogen Deposition, *Journal of Advances in Modeling Earth Systems*, 12, e2019MS002026, <https://doi.org/10.1029/2019MS002026>, e2019MS002026 10.1029/2019MS002026, 2020.
- Pirjola, L., O'Dowd, C. D., Brooks, I. M., and Kulmala, M.: Can new particle formation occur in the clean marine boundary layer?, *Journal of Geophysical Research: Atmospheres*, 105, 26 531–26 546, <https://doi.org/10.1029/2000JD900310>, 2000.
- Quinn, P. K. and Bates, T. S.: The case against climate regulation via oceanic phytoplankton sulphur emissions, *Nature*, 480, 51–56, <https://doi.org/10.1038/nature10580>, 2011.
- Roldin, P., Eriksson, A., Nordin, E., Hermansson, E., Taipale, D., Rusanen, A., Boy, M., Swietlicki, E., Svenningsson, B., Zelenyuk, A., and Pagels, J.: Modelling non-equilibrium secondary organic aerosol formation and evaporation with the aerosol dynamics, gas- and particle-phase chemistry kinetic multilayer model ADCHAM, *ATMOSPHERIC CHEMISTRY AND PHYSICS*, 14, 7953–7993, <https://doi.org/10.5194/acp-14-7953-2014>, 2014.



- 920 Rosati, B., Christiansen, S., Wollesen de Jonge, R., Roldin, P., Jensen, M. M., Wang, K., Moosakutty, S. P., Thomsen, D., Salomonsen, C., Hyttinen, N., Elm, J., Feilberg, A., Glasius, M., and Bilde, M.: New Particle Formation and Growth from Dimethyl Sulfide Oxidation by Hydroxyl Radicals, *ACS Earth and Space Chemistry*, 5, 801–811, <https://doi.org/10.1021/acsearthspacechem.0c00333>, 2021.
- Rosenfeld, D., Zhu, Y., Wang, M., Zheng, Y., Goren, T., and Yu, S.: Aerosol-driven droplet concentrations dominate coverage and water of oceanic low-level clouds, *Science*, 363, eaav0566, <https://doi.org/10.1126/science.aav0566>, 2019.
- 925 Salter, M. E., Zieger, P., Acosta Navarro, J. C., Grythe, H., Kirkevåg, A., Rosati, B., Riipinen, I., and Nilsson, E. D.: An empirically derived inorganic sea spray source function incorporating sea surface temperature, *Atmospheric Chemistry and Physics*, 15, 11 047–11 066, <https://doi.org/10.5194/acp-15-11047-2015>, 2015.
- Schmitz, G. and Elm, J.: Assessment of the DLPNO Binding Energies of Strongly Noncovalent Bonded Atmospheric Molecular Clusters, *ACS Omega*, 5, 7601–7612, <https://doi.org/10.1021/acsomega.0c00436>, 2020.
- 930 Shen, J., Scholz, W., He, X.-C., Zhou, P., Marie, G., Wang, M., Marten, R., Surdu, M., Rörup, B., Baalbaki, R., Amorim, A., Ataei, F., Bell, D. M., Bertozzi, B., Brasseur, Z., Caudillo, L., Chen, D., Chu, B., Dada, L., Duplissy, J., Finkenzeller, H., Granzin, M., Guida, R., Heinritzi, M., Hofbauer, V., Iyer, S., Kempainen, D., Kong, W., Krechmer, J. E., Kürten, A., Lamkaddam, H., Lee, C. P., Lopez, B., Mahfouz, N. G. A., Manninen, H. E., Massabò, D., Mauldin, R. L., Mentler, B., Müller, T., Pfeifer, J., Philippov, M., Piedehierro, A. A., Roldin, P., Schobesberger, S., Simon, M., Stolzenburg, D., Tham, Y. J., Tomé, A., Umo, N. S., Wang, D., Wang, Y., Weber, S. K., Welti, A., Wollesen de Jonge, R., Wu, Y., Zauner-Wieczorek, M., Züst, F., Baltensperger, U., Curtius, J., Flagan, R. C., Hansel, A., Möhler, O., Petäjä, T., Volkamer, R., Kulmala, M., Lehtipalo, K., Rissanen, M., Kirkby, J., El-Haddad, I., Bianchi, F., Sipilä, M., Donahue, N. M., and Worsnop, D. R.: High Gas-Phase Methanesulfonic Acid Production in the OH-Initiated Oxidation of Dimethyl Sulfide at Low Temperatures, *Environmental Science & Technology*, 56, 13 931–13 944, <https://doi.org/10.1021/acs.est.2c05154>, 2022.
- Slinn, S. and Slinn, W.: Predictions for particle deposition on natural waters, *Atmospheric Environment* (1967), 14, 1013–1016, [https://doi.org/https://doi.org/10.1016/0004-6981\(80\)90032-3](https://doi.org/https://doi.org/10.1016/0004-6981(80)90032-3), 1980.
- 940 Sofiev, M., Soares, J., Prank, M., de Leeuw, G., and Kukkonen, J.: A regional-to-global model of emission and transport of sea salt particles in the atmosphere, *Journal of Geophysical Research (Atmospheres)*, 116, 21 302–, <https://doi.org/10.1029/2010JD014713>, 2011.
- Turnipseed, A. A., Barone, S. B., Jensen, N. R., Hanson, D. R., Howard, C. J., and Ravishankara, A. R.: Kinetics of the Reactions of CF3O Radicals with CO and H2O, *The Journal of Physical Chemistry*, 99, 6000–6009, <https://doi.org/10.1021/j100016a041>, 1995.
- 945 Veres, P. R., Neuman, J. A., Bertram, T. H., Assaf, E., Wolfe, G. M., Williamson, C. J., Weinzierl, B., Tilmes, S., Thompson, C. R., Thames, A. B., Schroder, J. C., Saiz-Lopez, A., Rollins, A. W., Roberts, J. M., Price, D., Peischl, J., Nault, B. A., Møller, K. H., Miller, D. O., Meinardi, S., Li, Q., Lamarque, J.-F., Kupc, A., Kjaergaard, H. G., Kinnison, D., Jimenez, J. L., Jernigan, C. M., Hornbrook, R. S., Hills, A., Dollner, M., Day, D. A., Cuevas, C. A., Campuzano-Jost, P., Burkholder, J., Bui, T. P., Brune, W. H., Brown, S. S., Brock, C. A., Bourgeois, I., Blake, D. R., Apel, E. C., and Ryerson, T. B.: Global airborne sampling reveals a previously unobserved dimethyl sulfide oxidation mechanism in the marine atmosphere, *Proceedings of the National Academy of Sciences*, 117, 4505–4510, <https://doi.org/10.1073/pnas.1919344117>, 2020.
- 950 Wang, S., Newland, M., Deng, W., Rickard, A., Hamilton, J., Muñoz, A., Ródenas, M., Vázquez, M., Wang, L., and Wang, X.: Aromatic Photooxidation, A New Source of Atmospheric Acidity, *Environmental Science & Technology*, XXXX, <https://doi.org/10.1021/acs.est.0c00526>, 2020.
- 955 Wanninkhof, R.: Relationship between wind speed and gas exchange over the ocean revisited, *Limnology and Oceanography: Methods*, 12, 351–362, <https://doi.org/https://doi.org/10.4319/lom.2014.12.351>, 2014.



- 960 Wentworth, G. R., Murphy, J. G., Croft, B., Martin, R. V., Pierce, J. R., Côté, J.-S., Courchesne, I., Tremblay, J.-E., Gagnon, J., Thomas, J. L.,
Sharma, S., Toom-Saunry, D., Chivulescu, A., Lévasseur, M., and Abbatt, J. P. D.: Ammonia in the summertime Arctic marine boundary
layer: sources, sinks, and implications, *Atmospheric Chemistry and Physics*, 16, 1937–1953, <https://doi.org/10.5194/acp-16-1937-2016>,
2016.
- Werner, H.-J., Knowles, P. J., Manby, F. R., Black, J. A., Doll, K., Hesselmann, A., Kats, D., Kohn, A., Korona, T., Kreplin, D. A., Ma, Q.,
Miller, T. F. I., Mitrushchenkov, A., Peterson, K. A., Polyak, I., Rauhut, G., and Sibaev, M.: The Molpro quantum chemistry package,
Journal of Chemical Physics, 152, 144 107, 2020.
- Williamson, C. J., Kupc, A., Axisa, D., Bilsback, K. R., Bui, T., Campuzano-Jost, P., Dollner, M., Froyd, K. D., Hodshire, A. L., Jimenez,
965 J. L., Kodros, J. K., Luo, G., Murphy, D. M., Nault, B. A., Ray, E. A., Weinzierl, B., Wilson, J. C., Yu, F., Yu, P., Pierce, J. R.,
and Brock, C. A.: A large source of cloud condensation nuclei from new particle formation in the tropics, *Nature*, 574, 399–403,
<https://doi.org/10.1038/s41586-019-1638-9>, 2019.
- Wollesen de Jonge, R., Elm, J., Rosati, B., Christiansen, S., Hyttinen, N., Lüdemann, D., Bilde, M., and Roldin, P.: Secondary aerosol
formation from dimethyl sulfide – improved mechanistic understanding based on smog chamber experiments and modelling, *Atmospheric*
970 *Chemistry and Physics*, <https://doi.org/10.5194/acp-2020-1324>, 2021.
- Wollesen de Jonge, R., Xavier, C., Olenius, T., Elm, J., Svenhag, C., Hyttinen, N., Nieradzik, L., Sarnela, N., Kristensson, A., Petäjä, T., Ehn,
M., and Roldin, P.: Natural Marine Precursors Boost Continental New Particle Formation and Production of Cloud Condensation Nuclei,
Environmental Science & Technology, 58, 10956–10968, <https://doi.org/10.1021/acs.est.4c01891>, 2024.
- Wu, R., Wang, S., and Wang, L.: A New Mechanism for The Atmospheric Oxidation of Dimethyl Sulfide. The Importance of Intramolecular
975 Hydrogen Shift in CH₃SCH₂OO Radical., *The journal of physical chemistry. A*, 119, <https://doi.org/10.1021/jp511616j>, 2014.
- Ye, Q., Goss, M. B., Krechmer, J. E., Majluf, F., Zaytsev, A., Li, Y., Roscioli, J. R., Canagaratna, M., Keutsch, F. N., Heald, C. L., and
Kroll, J. H.: Product distribution, kinetics, and aerosol formation from the OH oxidation of dimethyl sulfide under different RO₂ regimes,
Atmospheric Chemistry and Physics, 22, 16003–16015, <https://doi.org/10.5194/acp-22-16003-2022>, 2022.
- Yin, F., Grosjean, D., Flagan, R. C., and Seinfeld, J. H.: Photooxidation of dimethyl sulfide and dimethyl disulfide. II: Mechanism evaluation,
980 *Journal of Atmospheric Chemistry*, 11, 365–399, <https://doi.org/10.1007/BF00053781>, 1990.
- Zhao, Y. and Truhlar, D.: The M06 suite of density functionals for main group thermochemistry, thermochemical kinetics, noncovalent
interactions, excited states, and transition elements: two new functionals and systematic testing of four M06 functionals and 12 other
functionals, *Theoretical Chemistry Accounts*, 120, 215–241, <https://doi.org/10.1007/s00214-007-0310-x>, 2008.
- Zheng, G., Wang, Y., Wood, R., Jensen, M. P., Kuang, C., McCoy, I. L., Matthews, A., Mei, F., Tomlinson, J. M., Shilling, J. E., Zawadowicz,
985 M. A., Crosbie, E., Moore, R., Ziemba, L., Andreae, M. O., and Wang, J.: New particle formation in the remote marine boundary layer,
Nature Communications, 12, 527, <https://doi.org/10.1038/s41467-020-20773-1>, 2021.
- Ziska, F., Quack, B., Abrahamsson, K., Archer, S. D., Atlas, E., Bell, T., Butler, J. H., Carpenter, L. J., Jones, C. E., Harris, N. R. P., Hepach,
H., Heumann, K. G., Hughes, C., Kuss, J., Krüger, K., Liss, P., Moore, R. M., Orlikowska, A., Raimund, S., Reeves, C. E., Reifenhäuser,
W., Robinson, A. D., Schall, C., Tanhua, T., Tegtmeier, S., Turner, S., Wang, L., Wallace, D., Williams, J., Yamamoto, H., Yvon-Lewis,
990 S., and Yokouchi, Y.: Global sea-to-air flux climatology for bromoform, dibromomethane and methyl iodide, *Atmospheric Chemistry and*
Physics, 13, 8915–8934, <https://doi.org/10.5194/acp-13-8915-2013>, 2013.